Title:

Biological characterization of breast cancer spheroid formed by fast fabrication method

Authors:

Yuta Iijima[1,2,3], Norino Uenaka[4], Mayu Morimoto[4], Daiki Sato[4], Satomi Hirose[3], Naoyoshi Sakitani[5,6,7], Masahiro Shinohara[6], Kenichi Funamoto[3,8], Gen Hayase[9]*, Daisuke Yoshino[2,4,5]*

Affiliations:

[1] Graduate School of Bio-Applications and Systems Engineering, Tokyo University of Agriculture and Technology, 2-24-16 Naka-cho, Koganei, Tokyo 184-8588, Japan

[2] Faculty of Engineering, Tokyo University of Agriculture and Technology, 2-24-16 Naka-cho, Koganei, Tokyo 184-8588, Japan

[3] Graduate School of Biomedical Engineering, Tohoku University, 6-6-12 Aramaki-aza-Aoba, Aoba-ku, Sendai, Miyagi 980-8579, Japan

[4] Graduate School of Engineering, Tokyo University of Agriculture and Technology, 2-24-16 Naka-cho, Koganei, Tokyo 184-8588, Japan

[5] Institute of Engineering, Tokyo University of Agriculture and Technology, 2-24-16 Naka-cho, Koganei, Tokyo 184-8588, Japan

[6] Department of Rehabilitation for Movement Functions, National Rehabilitation Center for Persons with Disabilities, 4-1 Namiki, Tokorozawa, Saitama 359-8555, Japan

[7] Department of Life Science and Biotechnology, National Institute of Advanced Industrial Science and Technology, 2217-4 Hayashi-cho, Takamatsu, Kagawa 761-0395, Japan

[8] Institute of Fluid Science, Tohoku University, 2-1-1 Katahira, Aoba-ku, Sendai, Miyagi 980-8577, Japan

[9] International Center for Materials Nanoarchitechtonics, National Institute for Materials Science, 1-1 Namiki, Tsukuba, Ibaraki 305-0044, Japan

Corresponding author (Lead author):

dyoshino@go.tuat.ac.jp (Daisuke Yoshino, Ph.D.)

Co-corresponding author:

gen@aerogel.jp (Gen Hayase, Ph.D.)

Abstract

Engineered three-dimensional (3D) tissue culture platforms are useful for reproducing and elucidating complex *in vivo* biological phenomena. Spheroids, 3D aggregates of living cells, are produced based on physicochemical or microfabrication technologies and are commonly used even in cancer pathology research. However, conventional methods have difficulties in constructing 3D structures depending on the cell types, and require specialized techniques/lab know-how to reproducibly control the spheroid size and shape. To overcome these issues, we have developed a fabrication method, which enables anyone to make and mature cancer spheroids using a superhydrophobic microwell made of the monolithic porous materials. Here, we characterize the biological behaviors of the breast cancer spheroids fabricated by our method under normoxic and hypoxic conditions. We found that the fabricated spheroid contracted to a certain size via activation of the actomyosin system. Cell proliferation induced a hypoxic state inside the spheroid (elevated expression of the hypoxia-inducible factor HIF-1α), followed by the formation of a necrotic core and cell escape from the spheroid. In addition, we observed a decrease in cancer spheroid contractility and cell escape from spheroids under hypoxic conditions compared to normoxic conditions, which were related to oxygen concentration-dependent cell motility. The fabricated spheroids perform as 3D tumor tissues in a highly reproducible manner and within a short culture period. Our findings indicate that this fabrication method has a wide range of applications in cancer research, such as elucidating the mechanisms of tumor invasion and metastasis and screening anticancer drugs, as with previous methods.

Keywords: Cancer spheroid; Fast fabrication; Superhydrophobic substrate; In vitro model; Hypoxia

Highlights

- Cancer spheroids of the desired size can be produced in a highly reproducible manner.
- The fabricated MDA-MB-231 spheroid contracts via actomyosin system activation.
- Cell proliferation induces a highly hypoxic state inside the spheroid.
- Necrotic core formation in the inner layer and cell escape from the spheroid can be reproduced.
- Spheroid behavior is influenced by oxygen concentration-dependent changes in cell motility.

Main Text:

Introduction

Engineered three-dimensional (3D) tissue culture platforms are useful tools for mimicking biological phenomena, replacing conventional tissue culture models with laboratory animals. These platforms can reproduce complex *in vivo* environments, such as cell-cell or cell-matrix interactions, mass transport, and cellular morphology and heterogeneity [1,2]. The study of cancer pathology is no exception, for which 3D tissue culture is required because conventional two-dimensional (2D) cell cultures weaken the malignant phenotype and cell-matrix crosstalk [3,4,5,6]. This has led to the development of various engineered culture platforms for cancer tissues.

Cancer cells grow and proliferate in a dense mass *in vivo*. The cellular spheroid formation is, therefore, one of the most common methods to reproduce cancer pathology *in vitro*. Recently proposed methods for the spheroid formation include microwells with surface modification to control cell adhesion [7,8], hanging drops or microfluidic devices based on microfabrication technology [2,9,10,11], and magnetic levitation using magnetic microbeads [12]. All of these methods can produce cellular spheroids in large quantities with high yields. However, they are not ready for use because they require a certain level of techniques to control the size and shape of the spheroid, and the protocol must be optimized according to the experiment to be handled. Considering the above-mentioned issues, we have developed a method to make tumor spheroids easily by using a superhydrophobic microwell processed from monolithic porous materials with a computer numerical control milling machine [13]. In our method, the tumor spheroids can be quickly fabricated by simply dispensing a cell/extracellular matrix (ECM) suspension on the microwell and incubating. The size of the spheroid is determined by the volume of the solution, which makes it easy to control, and not only can a large number of spheroids be formed at once, but it is also possible to apply this method to cell types that are difficult to form spheroids using conventional methods.

Here, we show the biological characterization of breast cancer spheroid produced using our fast fabrication method and its broad applicability to cancer research. To this end, we evaluated behaviors of the spheroids in normoxia as well as in hypoxia to which breast cancer tissue is exposed [14,15], both morphologically and at the protein levels. We found a contraction of the cancer spheroid to a certain size via the actomyosin system as the breast cancer cells in its inner layer proliferated over the culture duration. The spheroids exhibited increased expression of the hypoxia-inducible factor HIF-1α with cell proliferation, formation of a necrotic core in their inner layer, and escape of the cells from the spheroids. We also confirmed a delay in the spheroid contraction and cell escape from spheroids under hypoxic conditions compared to normoxic conditions, which were related to oxygen concentration-dependent cell motility.

Methods

Antibodies and chemicals. The primary and secondary antibodies used in this study are listed in **Supplementary Tables 1** and **2**. (S)-(-)-blebbistatin (blebbistatin; B592500) was purchased from Toronto Research Chemicals (Toronto, ON, Canada). Blebbistatin inhibits actomyosin contractility by blocking myosin II-dependent cell processes [16]. To inhibit actomyosin contractility, MDA-MB-

231 spheroids were incubated in the experimental medium containing 5 μM blebbistatin prepared with dimethyl sulfoxide (DMSO; Fujifilm Wako Pure Chemical Corporation, Osaka, Japan) from day 0. CultureSure® Y-27632 (Y-27632; 030-24021) was purchased from Fujifilm Wako Pure Chemical Corporation. For inhibition of Rho-associated protein kinase 1/2 (ROCK1/2) activity [17], MDA-MB-231 spheroids were cultured in the experimental medium containing Y-27632 at a final concentration of 5 μM from day 0.

Cell culture and spheroid formation. Green fluorescent protein (GFP)-labeled MDA-MB-231 cells (human breast adenocarcinoma cell line, AKR-201, Cell Biolabs, San Diego, CA, USA) were cultured in a 75 cm^2 flask (VTC-F75V, VIOLAMO, AS-ONE, Osaka, Japan) with Dulbecco's modified eagle medium (DMEM; 31600-034, Gibco, Thermo Fisher Scientific, Waltham, MA, USA) containing 10 v/v% heat-inactivated fetal bovine serum (S1810, BioWest, Nuaillé, France) and 1 v/v% penicillin-streptomycin (15140-122, Gibco). After reaching 90% confluence, the MDA-MB-231 cells were harvested with 0.25% trypsin-EDTA (25200-072, Gibco) and re-suspended in DMEM at the concentration of 5×10^7 cells/mL. Spheroids were then formed according to the protocols described in our previous work [13]. Cell-suspended collagen solution [4.0 mg/mL; native collagen acidic solution (IAC-50, KOKEN, Tokyo, Japan), 10× DMEM, 10 mM $NaHCO_3$, 10 mM HEPES-NaOH (pH7.5), and the cell suspension] was prepared on ice to give the final concentration of 5×10^6 cells/mL. The cell-suspended collagen solution was dispensed onto the superhydrophobic multiwell plate. The dispensed collagen solution was incubated at 37 ºC in a 100% humidified atmosphere of 5% CO_2 in air for 30–60 min. After gelation, the primary spheroids with 2 mm (for observation on dynamics and immunohistochemistry) or 5 mm (for immunoblotting) diameter were transferred to a 48-well plate (VTC-P48, VIOLAMO). For comparison, other cancer cell lines, MIA Paca2 (human pancreatic cancer cell line; RCB2094, RIKEN BioResource Research Center (BRC)), MCF7 (human breast adenocarcinoma cell line; RCB1902, RIKEN BRC), and HeLa (human cervical cancer cell line provided by Cell Resource Center for Biomedical Research, Institute of Development, Aging and Cancer, Tohoku University, Japan) were cultured under the same conditions, and spheroids were prepared from these cell lines.

Hypoxic exposure. Constructed MDA-MB-231 spheroids were then exposed to normoxia (21% O_2) or hypoxia (5% O_2 and 3% O_2) balanced with 5% CO_2 and N_2 at 37 ºC in a multi-gas incubator (MCO-5MUV; PHC Corporation, Tokyo, Japan). The spheroids were cultured from day 0, the day they were made, until day 15. Dynamics in the spheroids were observed daily with phase-contrast microscopy (CKX43 or CKX53, Olympus, Tokyo, Japan). The diameter of the spheroid was measured using ImageJ [18] based on the obtained phase-contrast images.

Immunohistochemistry. Cultured MDA-MB-231 spheroids were fixed with 4% paraformaldehyde phosphate buffer saline (PFA; 163-20145, Fujifilm Wako Pure Chemical Corporation, Osaka, Japan) for 3 h at 4 °C. The spheroids were cryoprotected by soaking in 20 w/v% sucrose/phosphate buffered saline (PBS; 05913, Nissui Pharmaceutical, Tokyo, Japan) for 5 h and 30 w/v% sucrose/PBS for an additional overnight at 4 °C. Fixed spheroids were frozen in optimal cutting temperature (OCT) compound (45833, Sakura Finetek Japan, Tokyo, Japan) and

cut into 10 or 15 μm-thick frozen sections on cryofilm using a cryostat (CM3050S or CM1860; Leica Microsystems, Wetzlar, Germany). After cutting out the frozen sections, the MDA-MB-231 cells were permeabilized with 0.1% Triton X-100 (17-1315-01, Pharmacia Biotech, Uppsala, Sweden) in Tris-buffered saline (TBS), followed by incubation in 1% Block Ace (BA; UKB40, DS Pharma Biomedical, Osaka, Japan) in TBS to prevent nonspecific antibody absorption. The cells were then stained using the primary and secondary antibodies diluted in 1% BA in PBS and PBS, respectively, at predefined concentrations. (**Supplementary Tables 1** and **2**). Cell nuclei and actin cytoskeleton were stained using 4',6-diamidino-2-phenylindole dihydrochloride (DAPI; D1306, Invitrogen, Thermo Fisher Scientific) and Alexa Fluor 633 phalloidin (A22284, Invitrogen, Thermo Fisher Scientific), respectively. Stained MDA-MB-231 spheroid sections were observed using a wide-field fluorescence microscope (BZ-9000 or BZ-X810, Keyence, Osaka, Japan).

Protein extraction. Protein extraction samples were prepared according to the following protocol. Whole-cell lysate was obtained by collecting the supernatant after washing with ice-cold PBS, mashing, and incubating the spheroids in lysis buffer [50 mM Tris-HCl (pH7.4), 150 mM NaCl, 1% TritonX-100, 1% SDS, 10 mM EDTA, 1 mM Na_3VO_4, 10 mM NaF, 20 mM DTT, and protease inhibitor cocktail (P8340, Sigma-Aldrich)] on ice for 5 min, and centrifugation at 20,000 *g*, 4 ºC for 10 min. Each sample was boiled for 5 min after adding 4× Laemmli Sample Buffer (161-0747, Bio-Rad Laboratories, Hercules, CA, USA).

Immunoblotting. Samples were subjected to SDS-PAGE and then transferred onto the Immun-Blot PVDF membrane (162-0177, Bio-Rad Laboratories). The membrane was blocked with TBS containing 1% BA and 0.05% Tween 20 to reduce the background noise. The membrane was then stained using primary and secondary antibodies diluted in Can Get Signal Immunoreaction Enhancer Solution (NKB-101, Toyobo, Osaka, Japan) at predefined concentrations (**Supplementary Tables 1** and **2**). The blotted proteins were detected and visualized using Clarity Max Western ECL Substrate (170-5062, Bio-Rad Laboratories). Protein loading was monitored using loading control proteins (*i.e.*, α-tubulin and β-actin). The molecular weight of each protein was determined based on Precision Plus Protein Dual Color Standards (161-0374, Bio-Rad Laboratories). The density of protein bands on immunoblots was determined using Image Lab (170–9691, Bio-Rad Laboratories).

Evaluation of cell escape from spheroids. A base was prepared by adding 100 μL of collagen solution [1.5 mg/mL; native collagen acidic solution (IAC-50), 10× DMEM, 10 mM $NaHCO_3$, 10 mM HEPES-NaOH (pH7.5), and H_2O] to the 48-well plate and incubating at 37 ºC for 30–45 min to turn into a gel. The spheroid immediately after fabrication was placed in the center of the base, and 200 μL of the collagen solution (1.5 mg/mL) was gently added to embed the spheroid in the collagen gel. After gelation, 500 μL of the culture medium was added, and the spheroid was incubated under each oxygen concentration. The dynamics of cells escaping from the spheroids were observed daily by phase contrast microscopy. Based on the captured images, the maximum distance that the escaped cells spread to the surrounding gel was measured using ImageJ, and

the mean distance that the cells spread was calculated by dividing the area where cells escaped by the perimeter of the spheroid.

Quantification of protein distribution in spheroids. Fluorescence intensity distributions for each protein were obtained from the fluorescence-stained images using the ImageJ plug-in (**Supplementary Source Code 1**), which can extract pixel-by-pixel coordinates and intensity values for regions of interest. Frozen sections of spheroids were then plotted on a unit circle, and the obtained fluorescence intensity distribution was divided into regions of 20% radius and normalized over the intensity value in the central 20% to allow comparison of different section images. The rate of Ki-67-positive cells was calculated by dividing the number of cells expressing Ki-67 by the total number of cells counted by cell nuclei.

Statistics and reproducibility. All values are shown as mean ± standard deviation (SD) unless stated otherwise. Each data was obtained from three independently repeated experiments. Statistical analysis was performed using the two-sided Welch's *t*-test for comparisons of two groups and the one-way ANOVA or two-way ANOVA, followed by the two-sided multiple comparison test (Dunnett's test or Tukey-Kramer test), with statistical significance set at $p < 0.1$ (marginally significant), $p < 0.05$, and $p < 0.01$ (significant difference).

Mathematical modeling and calculation. To estimate the oxygen concentration inside a spheroid, we formulated a mathematical model for the diffusion dynamics of oxygen. Assuming that cells consume oxygen as it diffuses into the center of the spheroid, we used the mass transfer equation for diffusive transport with simultaneous consumption shown below, with reference to the previous study [19, 20]. The model was deemed to be spherically symmetric concerning the center of the spheroid, and the changes in oxygen occurred only in one-dimensional radial coordinates and were independent of polar and azimuthal angles.

$$\frac{\partial C}{\partial t} = D\frac{\partial^2 C}{\partial r^2} - \psi$$

where C is the oxygen concentration; t is time; r is the radial coordinate of the spheroid; D is the binary diffusion coefficient; and ψ is the oxygen consumption. To extract the line component in the radial direction of the spheroid, a 2-mm straight line was divided into elements by 20 divisions, assuming oxygen concentration gradient-dependent exchange between adjacent elements, and the concentration in each element was calculated every one minute. As initial conditions, all elements were input the amount of oxygen supplied to the spheroid from the culture medium obtained based on oxygen solubility in water at atmospheric pressure [19, 21]: 267.0 μmol/L (21% O_2), 63.6 μmol/L (5% O_2), and 38.1 μmol/L (3% O_2), respectively. The diffusion coefficient of oxygen was set to 2.0×10^{-9} m^2/s [20]. Oxygen consumption was determined by multiplying the number of cells in the spheroid by the consumption rate per cell, 5.5×10^{-15} mol/(cell·s) [22]. The number of cells in the spheroids was calculated from the cell concentration at the time of spheroid fabrication (5×10^6 cells/mL; 4.8 μL per spheroid), assuming that the number of cells doubled or increased 1.5-fold in one day. We calculated oxygen consumption for 15 days of culture, updating

the oxygen consumption every 24 hours, with the assumption that there is no cell proliferation in the inner layer of the spheroid after day 7, based on observation of cell dynamics by fluorescent staining. Under conditions in which MDA-MB-231 cells form a shell-like layer on the spheroid surface, the amount of oxygen supplied from the outside to the inside of the spheroid was independently calculated from 1/4 to 1/10 based on the oxygen permeability. The permeability of the plasma membrane or lipid bilayer is known to be two to three times lower than that of a water layer of the same thickness [23, 24]. The obtained value was given as a boundary condition to the element corresponding to the spheroid surface as the oxygen supply.

Results

Cellular dynamics in the MDA-MB-231 spheroid.

We first examined the behavior of MDA-MB-231 cells in fast-fabricated spheroids for 15 days. As in the previous study [13], rapid contraction of spheroids was observed around day 2 after fabrication (**Fig. 1a**). The spheroids then contracted slowly around day 5 and shrank to approximately 60% of their original size by day 15 (**Fig. 1b**). On the other hand, spheroids were easily fabricated using other cancer cell types, but we did not observe the spheroid contraction observed when using MDA-MB-231 cells (**Supplementary Fig. 1**). We also sighted the cells inside the spheroid during the 15-day incubation period by making the frozen sections, and confirmed an increase in cell density along with culture duration, the formation of an outer shell-like dense cell area around day 6, and quenching of GFP expressed by the cells in the center of the spheroid from around day 11 (**Fig. 1c**). The presence of cell nuclei, which we could confirm by DAPI staining, suggests that cell death was induced rather than a decrease in cell density inside the spheroid. Especially after day 14, the GFP quenching was pronounced, indicating the formation of a necrotic core. The dense outer shell formed by the cells inhibited the delivery of oxygen and nutrients to the inside of the spheroid (**Supplementary Fig. 2**), and this fact may have contributed to the necrotic core formation. This notion is supported by our findings indicating dynamics in the expression of HIF-1α and activation of caspase-3 (*i.e.,* increase in the expression of cleaved caspase-3) in the spheroid (**Figs. 1d**–**1g, and 1i–1l**), which is observed during necrotic core formation [25, 26]. The expression level of HIF-1α showed an increasing trend from around day 7, increased significantly on day 9, and then decreased to near the original level (the level on day 3) toward day 15 (**Figs. 1d** and **1e**). In addition, we can see the localization of MDA-MB-231 cells with high fluorescence intensity of HIF-1α in the outer 20–40% of the spheroid around day 7 (**Figs. 1f** and **1g**). Similarly, we observed that the expression of vascular endothelial growth factor (VEGF-A) in the cells was localized from the entire spheroid to the outer layer (**Figs. 1f** and **1h**). The expression of cleaved caspase-3 tended to increase toward day 13 (**Figs. 1i** and **1j**), and the cells, in which caspase-3 was activated, were strongly localized to the outer layer of the spheroid but were also relatively distributed to the inner layer between days 5 and 13 (**Figs. 1k** and **1l**). Focusing on the distribution of Ki-67 positive cells and their percentage (**Figs. 1m** and **1n**), we can draw the conclusion that a necrotic core was formed in the inner layer the spheroid based on the transition of cells with the proliferative potential to the outer layer of the spheroid with each day of

culture. These data demonstrate that, in general, the fabricated spheroids behave as 3D tumor tissues as in the previous studies [26, 27, 28], except for their contraction inherent to our method.

Actomyosin contractility plays a critical role in the MDA-MB-231 spheroid contraction.
We then sought a factor that contributes to the contraction of the fast fabricated MDA-MB-231 spheroids. We focused on two aspects of cellular traction force through the collagen network and degradation of the ECM by the cells, given the lack of size changes in the collagen spheres themselves over time [13].

The contractility of the actomyosin system involved in traction force, *i.e.*, F-actin expression and myosin light chain 2 phosphorylation (pMLC), tended to be higher on day 3 (and day 5 for pMLC) when the rapid spheroid contraction was observed (**Figs. 2a**, **2b**, **2c**, and **Supplementary Fig. 3**). The expression level of F-actin increased again in the late stage of spheroid culture duration (after day 11; **Fig. 2b**). In MDA-MB-231 cells located in the outer 20-40% of the spheroid, phosphorylation of MLC was observed to co-localize with F-actin from day 3, and its distribution state continued until day 7 (**Figs. 2d** and **2e**). These results indicate that the activation of the actomyosin contractility is consistent with the rapid spheroid contraction on the time scale.

The expression of matrix metalloproteinase (MMP)-9, which acts as a degrading enzyme of ECM, tended to increase in the middle stage of culture duration (day 9; **Figs. 2f** and **2g**). MMP-2, an enzyme that plays an important role in cancer invasion and metastasis similar to MMP-9, tended to increase expression of its active form (64 kDa) after an increase in its proenzyme form (72 kDa) (**Figs. 2h** and **2i**). However, no significant differences in the expressions of MMP-9 and MMP-2 were observed during the culture duration in this study. Hence, the contraction of MDA-MB-231 spheroids in this study is poorly related to ECM degradation.

To clarify the causal relationship between rapid spheroid contraction and the actomyosin system, we inhibited actomyosin activity with blebbistatin. The MDA-MB-231 spheroid no longer exhibited rapid contraction from day 2 to day 5, whereas long-term continuous contraction was not suppressed (**Figs. 2j** and **2k**). Cell proliferation within the spheroid was not significantly affected by exposure to blebbistatin, as evidenced by the fact that the intensity of transmitted light in phase-contrast images decreased with culture time (**Fig. 2j**). We, therefore, conclude that actomyosin contractility is one of the factors causing contraction (especially rapid contraction) of MDA-MB-231 spheroids.

MDA-MB-231 spheroid contraction over time is delayed in high hypoxia.
We then examined the behavior of the fabricated MDA-MB-231 spheroids under physiological hypoxic conditions (oxygen concentration: 5% or 3% O_2). High hypoxia (3% O_2) induced a delay in the rapid contraction of spheroids from day 2 to day 5, which was observed under normoxia (21% O_2) (**Figs. 3a, 3b**, and **3c**). The highly hypoxic condition also slowed the increase in cell density (*i.e.*, decrease in mean gray value based on transmitted light intensity) along with the delayed contraction of the spheroid (**Fig. 3d**). We hypothesized that the cause of these delays may be the enhanced migration of MDA-MB-231 cells exposed to the highly hypoxic condition. This hypothesis is supported by the observation that cells escaped from spheroids relatively early under hypoxic conditions. (**Fig. 3e**).

To allow observation of cells escaping from the spheroids, we investigated the cause of the delayed contraction of the spheroids by embedding them in collagen gels immediately after preparation. Under each oxygen condition, MDA-MB-231 cells were observed to escape from the spheroid and migrate into the surrounding gel over the culture durations (**Figs. 4a** and **4b**). The maximum and average distances at which MDA-MB-231 cells escaped from the spheroid were measured, indicating that the escape was significantly faster in the mild hypoxic condition (5% O_2) than in the other oxygen conditions (**Figs. 4c** and **4d**). MDA-MB-231 cells are known to differ in their migration depending on the oxygen concentration. Previous studies have shown that the 5% O_2 condition increased the cell migration speed compared to normoxia, whereas the 3% O_2 condition significantly increased the migration speed compared to normoxia, but less than the increase under the 5% O_2 condition [29]. Our results, therefore, suggest that the delayed contraction of spheroids in the highly hypoxic condition (3% O_2) is not due to hypoxia-induced enhancement of cell migration, but rather to reduced cell motility.

To further investigate the relationship between delayed spheroid contraction and cell motility, we evaluated the expression and activation state of the relevant proteins. The expression of HIF-1α showed an early increase in the mild hypoxic condition (5% O_2; day 3), whereas the increase tended to be delayed in the highly hypoxic condition (3% O_2; day 5) (**Figs. 5a** and **5b**). For the distributions of HIF-1α and VEGF-A, oxygen concentration did not affect the transition in their localization within spheroids (**Supplementary Fig. 4**). MMPs are involved in multiple stages of tumor invasion and metastasis. We thus analyzed expression changes of MMP-9 and MMP-2 in the MDA-MB-231 cells under each oxygen concentration. MMP-9 tended to increase on days 3 and 5, and to decrease on days 7 and 9 under the 5% O_2 condition, but there were no significant changes in its expression leading to the delay in the spheroid contraction under the 3% O_2 condition (**Supplementary Fig. 5**). In contrast, hypoxia induced a significant decrease in the expression of its active MMP-2 (64 kDa) (**Figs. 5c** and **5d**); in conjunction with a trend toward increased expression of its proenzyme form (72 kDa), the active MMP-2 began to increase on day 7 under the 5% O_2 condition, while its expression remained suppressed under the 3% O_2 conditions. We then examined the effect of hypoxia on the expression of lysyl oxidase (LOX), a cross-linking enzyme that has been shown to drive metastasis of some breast cancers to bone [30] and regulates breast cancer cell migration and adhesion [31]. Neither glycosylated (58 kDa) nor mature (32 kDa) LOXs showed significant changes in their expressions that might be responsible for the delay in the spheroid contraction (**Supplementary Fig. 6**). In addition, collagen type 1 (COL1A) and type 3 (COL3A1), the ECMs produced by MDA-MB-231 cells showed no significant oxygen concentration-dependent changes in distribution and amount (**Supplementary Fig. 7**). These results are hardly a specific response to the highly hypoxic condition; the persistent decreased expression of active MMP-2 in MDA-MB-231 cells may be associated with delayed spheroid contraction under the 3% O_2 conditions, but it is not a critical factor. Cells also show changes in their motility, including actin polymerization and actomyosin contractility, through the activation of Rac1 or RhoA, one of the small GTPases, and ROCK1/2 [32, 32, 34]. The expression levels of ROCK1/2 expression levels were slightly altered but were largely unaffected by oxygen concentration (**Supplementary Fig. 8**). In contrast, activation of the actomyosin system

(phosphorylation of MLC) tended to decrease under hypoxic conditions, although there was a large variation (**Figs. 5e**, **5f**, and **Supplementary Fig. 9**). Based on these findings, we concluded that the function of the actomyosin system is inhibited by indirect effects and evaluated spheroid dynamics using ROCK1/2 inhibitors. As a result, the MDA-MB-231 spheroid expanded slightly once and then contracted (**Figs. 5g**, **5h**, and **5i**). This phenomenon is similar to the delay in the spheroid contraction observed in the highly hypoxic condition. Our results conclude that the spheroids' delayed contraction was caused by reduced cell motility under the 3% O_2 condition. This notion is supported by the finding that the rate of Ki-67-positive cells tends to decrease early under the 3% O_2 conditions (**Supplementary Fig. 10**).

Discussion

In this study, we characterized behaviors in breast cancer spheroid produced using our fast fabrication method morphologically and at the protein levels. The fabricated spheroids generally perform as well as those with the previous studies do [26, 27, 28] as 3D tumor tissues, except for their contraction inherent to our method. This method also enables us to produce and mature spheroids of the desired size (even several millimeters in diameter) in a highly reproducible manner and within a short culture period (in about five days) by adjusting the cell suspension volume only. We, thus, anticipate that this spheroid fabrication has a wide range of applications in cancer research, such as elucidating the mechanisms of tumor invasion and metastasis and screening anticancer drugs.

Maturation of the spheroid, *i.e.*, an increase in internal cell density, led to hypoxia and induced HIF-1α expression, followed by the formation of a necrotic core in its center, accompanied by activation of Caspase-3 (**Fig. 1**). We also observed that tumor cells with high proliferative potential (the Ki-67 positive cells) transitioned to the outer layer of the spheroid with culture duration. These responses have been confirmed in conventional methods [26, 35] and in tissues *in vivo* [36]. Our findings, therefore, demonstrate that the spheroids fabricated in this study reproduce tumor dynamics in the cancer microenvironment. On the other hand, the fabricated spheroids have engineered organoid-like features with collagen as the structural backbone, and thus appear to undergo their contraction caused by the actomyosin contractility in MDA-MB-231 cells (**Fig. 2**). The spheroid contraction is not confirmed in the conventional fabrication without ECMs as the substrate. That alarming problem in our method can be avoided by using hydrogels whose main composition is ECMs other than collagen, for example gelatin methacrylate [37] or fibrin [38], as the structural foundation. Organoid-like spheroid fabricated by the present method can form aggregates similar to tissue *in vivo*, even for cell types that are difficult to structure in 3D by conventional methods (**Supplementary Fig. 1**). This advantage is conducive to the field of cancer research, even in light of the issue about spheroid contraction.

We observed some differences in the behavior of the fabricated spheroids under normoxic and hypoxic conditions in terms of their contraction and cellular escape from them (**Figs. 3** and **4**). The behavior of the spheroid-forming tumor cells under hypoxic conditions involves not only small GTPase [32, 33] and MMPs [39, 40] but also various proteins [41, 42]. In this study, we focused on some of those proteins and found that proteins related to cell motility are responsible for the

observed differences in spheroid behavior (**Fig. 5**). However, this study did not demonstrate the details of the mechanism leading to the differences. Further studies that provide a comprehensive analysis of the functions and interactions of those proteins are therefore needed in order to elucidate the full picture of the behavior in the fabricated spheroids.

The spheroid fabricated in this study, even a few mm in size, matures relatively early (about five days), independent of its size. In contrast, conventional methods require more than ten days to increase the size to the same level [43, 44, 45]. However, tumor spheroids produced by our method begin to form a necrotic core in the inner layer in about ten days, making them unsuitable for long-term culture. This is due to the fact that the MDA-MB-231 cells form a shell-like layer on the surface of the spheroid during the maturation process, inhibiting the supply of oxygen and nutrients to the inside of the spheroid and exposing most cells to a harsh environment (**Supplementary Fig. 2**). This notion is supported by the findings regarding the elevated HIF-1α expression levels of MDA-MB-231 cells in the spheroid under normoxic conditions (**Figs. 1d** and **1e**). To solve this problem, it is necessary to place tumor vessels inside the spheroid to provide a pathway for oxygen and nutrients. Our method can address this by pre-mixing the ECM with vascular endothelial cells and tumor cells.

Data availability

The authors declare that all data supporting the findings of this study are available within this article and its supplementary information files or from the corresponding author upon reasonable request.

Acknowledgments

The human pancreatic cancer cell line, MIA Paca2 (RCB2094) and human breast adenocarcinoma cell line, MCF7 (RCB1902), were provided by the RIKEN BRC through the National Bio-Resource Project of the MEXT/AMED, Japan. We thank Dr. Yoshitsugu Aoki, Director of the Department of Molecular Therapy, National Center of Neurology and Psychiatry, for providing the fluorescence microscope system. This study was partly supported by grants from the Nakatani Foundation for Advancement of Measuring Technologies in Biomedical Engineering and the JSPS KAKENHI (No. 21K19893) to D.Y.

Author contributions

D.Y. conceived and designed the research. Y.I. conducted most of the experiments. N.U. was in charge of most of the immunoblotting. M.M. and D.S. conducted mathematical modeling and calculation for oxygen concentration in spheroids. Y.I. and S.H. performed the analysis of the distribution of protein fluorescence intensity. N.S. and M.S. provided technical support in Immunohistochemistry. K.F. supported technical methods for hypoxic exposure experiments on cancer spheroids. G.H. developed, prepared, and provided the superhydrophobic substrates for spheroid fabrication. All authors discussed the data. Y.I. and D.Y. wrote the manuscript. D.Y. directed and supervised the project.

Declarations

Competing interests

The authors have no conflicts of interest directly relevant to the content of this article.

References

[1] Asghar W, Assal RE, Shafiee H, Pitteri S, Paulmurugan R, Demirci U. Engineering cancer microenvironments for *in vitro* 3-D tumor models. Mater Today. 2015; 18: 539–553. https://doi.org/10.1016/j.mattod.2015.05.002

[2] Kuo CT, Wang JY, Lin YF, Wo AM, Chen BPC, Lee H. Three-dimensional spheroid culture targeting versatile tissue bioassay using a PDMS-based hanging drop array. Sci Rep. 2017; 7: 4363. https://doi.org/10.1038/s41598-017-04718-1

[3] Lin RZ, Chang HY. Recent advances in three-dimensional multicellular spheroid culture for biomedical research. Biotechnol J. 2008; 3: 1172–1184. https://doi.org/10.1002/biot.200700228

[4] Thoma CR, Zimmermann M, Agarkova I, Kelm JM, Krek W. 3D cell culture systems modeling tumor growth determinants in cancer target discovery. Adv Drug Deliv Rev. 2014; 69–70: 29-41. https://doi.org/10.1016/j.addr.2014.03.001

[5] Nath S, Devi GR. Three-dimensional culture systems in cancer research: Focus on tumor spheroid model. Pharmacol Ther. 2016; 163: 94–108. https://doi.org/10.1016/j.pharmthera.2016.03.013

[6] Kapałczyńska M, Kolenda T, Przybyła W, Zajączkowska M, Teresiak A, Filas V, Ibbs M, Bliźniak R, Łuczewski Ł, Lamperska K. 2D and 3D cell cultures – a comparison of different types of cancer cell cultures. Arch Med Sci. 2018; 14: 910–919. https://doi.org/10.5114/aoms.2016.63743

[7] Stock K, Estrada MF, Vidic S, Gjerde K, Rudisch A, Santo VE, Barbier M, Bolm S, Arundkar SC, Selvam I, Osswald A, Stein Y, Gruenewald S, Brito C, van Weerden W, Rotter V, Boghaert E, Oren M, Sommergruber W, Chong Y, de Hoogt R, Graeser R. Capturing tumor complexity in vitro: Comparative analysis of 2D and 3D tumor models for drug discovery. Sci Rep. 2016; 6: 28951. https://doi.org/10.1038/srep28951

[8] Thermo Fisher Scientific, Inc., 3D cell culture protocols. 2023. https://www.thermofisher.com/jp/ja/home/references/protocols/cell-culture/3-d-cell-culture-protocol.html. Accessed 13 Mar 2023.

[9] Gao B, Jing C, Ng K, Pingguan-Murphy B, Yang Q, Fabrication of three-dimensional islet models by the geometry-controlled hanging-drop method. Acta Mech Sin. 2019; 35: 329–337. https://doi.org/10.1007/s10409-019-00856-z

[10] Marimuthu M, Rousset N, St-Georges-Robillard A, Lateef MA, Ferland M, Mes-Masson AM, Gervais T. Multi-size spheroid formation using microfluidic funnels. Lab Chip. 2018; 18: 304–314. https://doi.org/10.1039/C7LC00970D

[11] Moshksayan K, Kashaninejad N, Warkiani ME, Lock JG, Moghadas H, Firoozabadi B, Saidi MS, Nguyen NT. Spheroids-on-a-chip: Recent advances and design considerations in microfluidic platforms for spheroid formation and culture. Sens Actuators B Chem. 2018; 263: 151–176. https://doi.org/10.1016/j.snb.2018.01.223

[12] Haisler WL, Timm DM, Gage JA, Tseng H, Killian TC, Souza GR. Three-dimensional cell culturing by magnetic levitation. Nat Protoc. 2013; 8: 1940–1949. https://doi.org/10.1038/nprot.2013.125
[13] Hayase G, Yoshino D. CNC-milled superhydrophobic macroporous monoliths for 3D cell culture. ACS Appl Bio Mater. 2020; 3: 4747–4750. https://doi.org/10.1021/acsabm.0c00719
[14] McKeown SR. Defining normoxia, physoxia and hypoxia in tumours-implications for treatment response. Br J Radiol. 2014; 87: 20130676. https://doi.org/10.1259/bjr.20130676
[15] Palacio-Castañeda V, Velthuijs N, Le Gac S, Verdurmen WPR. Oxygen control: the often overlooked but essential piece to create better in vitro systems. Lab Chip. 2022; 22: 1068–1092. https://doi.org/10.1039/D1LC00603G
[16] Straight AF, Cheung A, Limouze J, Chen I, Westwood NJ, Sellers JR, Mitchison TJ. Dissecting temporal and spatial control of cytokinesis with a myosin II Inhibitor. Science. 2003; 299: 1743–1747. https://doi.org/10.1126/science.1081412
[17] Uehata M, Ishizaki T, Satoh H, Ono T, Kawahara T, Morishita T, Tamakawa H, Yamagami K, Inui J, Maekawa M, Narumiya S. Calcium sensitization of smooth muscle mediated by a Rho-associated protein kinase in hypertension. Nature. 1997; 389: 990–994. https://doi.org/10.1038/40187
[18] Schneider CA, Rasband WS, Eliceiri KW, NIH Image to ImageJ: 25 years of image analysis. Nat Methods. 2012; 9: 671–675. https://doi.org/10.1038/nmeth.2089
[19] Murphy KC, Hung BP, Browne-Bourne S, Zhou D, Yeung J, Genetos DC, Leach JK. Measurement of oxygen tension within mesenchymal stem cell spheroids. J R Soc Interface. 2017; 14: 20160851. https://doi.org/10.1098/rsif.2016.0851
[20] Grimes DR, Kelly C, Bloch K, Partridge M. A method for estimating the oxygen consumption rate in multicellular tumour spheroids. J R Soc Interface. 2014; 11: 20131124. https://doi.org/10.1098/rsif.2013.1124
[21] Xing W, Yin M, Lv Q, Hu Y, Liu C, Zhang J. Oxygen solubility, diffusion coefficient, and solution viscosity. In: Xing W, Yin G, Zhang J, editors. Rotating Electrode Methods and Oxygen Reduction Electrocatalysts. Elsevier; 2014. pp. 1–31. https://doi.org/10.1016/B978-0-444-63278-4.00001-X
[22] McMurtrey RJ. Analytic models of oxygen and nutrient diffusion, metabolism dynamics, and architecture optimization in three-dimensional tissue constructs with applications and insights in cerebral organoids. Tissue Eng Part C Methods. 2016; 22: 221–249. https://doi.org/10.1089/ten.tec.2015.0375
[23] Subczynski WK, Hopwood LE, Hyde JS. Is the mammalian cell plasma membrane a barrier to oxygen transport? J Gen Physiol. 1992; 100: 69–87. https://doi.org/10.1085/jgp.100.1.69
[24] Dotson RJ, McClenahan E, Pias SC. Updated evaluation of cholesterol's influence on membrane oxygen permeability. In: Nemoto EM, Harrison EM, Pias SC, Bragin DE, Harrison DK, LaManna JC, editors. Oxygen Transport to Tissue XLII. Advances in Experimental Medicine and Biology, vol 1269. Springer, Cham; 2021. 23–30. https://doi.org/10.1007/978-3-030-48238-1_4

[25] Riffle S, Pandey RN, Albert M, Hegde RS. Linking hypoxia, DNA damage and proliferation in multicellular tumor spheroids. BMC Cancer. 2017; 17: 338. https://doi.org/10.1186/s12885-017-3319-0
[26] Costa EC, Moreira AF, de Melo-Diogo D, Gaspar VM, Carvalho MP, Correia IJ. 3D tumor spheroids: an overview on the tools and techniques used for their analysis. Biotechnol Adv. 2016; 34: 1427–1441. https://doi.org/10.1016/j.biotechadv.2016.11.002
[27] Zhao L, Xiu J, Liu Y, Zhang T, Pan W, Zheng X, Zhang X. A 3D printed hanging drop dripper for tumor spheroids analysis without recovery. Sci Rep. 2019; 9: 19717. https://doi.org/10.1038/s41598-019-56241-0
[28] Ham SL, Joshi R, Luker GD, Tavana H. Engineered breast cancer cell spheroids reproduce biologic properties of solid tumors. Adv Healthc Mater. 2016; 5: 2788–2798. https://doi.org/10.1002/adhm.201600644
[29] Koens R, Tabata Y, Serrano JC, Aratake S, Yoshino D, Kamm RD, Funamoto K. Microfluidic platform for three-dimensional cell culture under spatiotemporal heterogeneity of oxygen tension. APL Bioeng. 2020; 4: 016106. https://doi.org/10.1063/1.5127069
[30] Cox TR, Rumney RMH, Schoof EM, Perryman L, Høye AM, Agrawal A, Bird D, Latif NA, Forrest H, Evans HR, Huggins ID, Lang G, Linding R, Gartland A, Erler JT. The hypoxic cancer secretome induces pre-metastatic bone lesions through lysyl oxidase. Nature. 2015; 552: 106–110. https://doi.org/10.1038/nature14492
[31] Payne SL, Fogelgren B, Hess AR, Seftor EA, Wiley EL, Fong SFT, Csiszar K, Hendrix MJC, Krischmann DA. Lysyl oxidase regulates breast cancer cell migration and adhesion through a hydrogen peroxide-mediated mechanism. Cancer Res. 2005; 65: 11429–11436. https://doi.org/10.1158/0008-5472.CAN-05-1274
[32] Xu H, Yuan Y, Wu W, Zhou M, Jiang Q, Niu L, Ji J, Liu N, Zhang L, Wang X. Hypoxia stimulates invasion and migration of human cervical cancer cell lines HeLa/SiHa through the Rab11 trafficking of integrin αvβ3/FAK/PI3K pathway-mediated Rac1 activation. J Biosci. 2017; 42: 491–499. https://doi.org/10.1007/s12038-017-9699-0
[33] Silva P, Mendoza P, Rivas S, Díaz J, Moraga C, Quest AFG, Torres VA. Hypoxia promotes Rab5 activation, leading to tumor cell migration, invasion and metastasis. Oncotarget. 2016; 7: 29548–29562. https://doi.org/10.18632/oncotarget.8794
[34] Chin VT, Nagrial AM, Chou A, Biankin AV, Gill AJ, Timpson P, Pajic M. Rho-associated kinase signalling and the cancer microenvironment: novel biological implications and therapeutic opportunities. Expert Rev Mol Med. 2015; 17: E17. https://doi.org/10.1017/erm.2015.17
[35] Close DA, Johnston PA. Detection and impact of hypoxic regions in multicellular tumor spheroid cultures formed by head and neck squamous cell carcinoma cells lines. SLAS Discov. 2022; 22: 39–54. https://doi.org/10.1016/j.slasd.2021.10.008
[36] Vleugel MM, Greijer AE, Shvarts A, van der Groep P, van Berkel M, Aarbodem Y, van Tinteren H, Harris AL, van Diest PJ, van der Wall E. Differential prognostic impact of hypoxia induced and diffuse HIF-1alpha expression in invasive breast cancer. J Clin Pathol. 2005; 58: 172–177. https://doi.org/10.1136/jcp.2004.019885

[37] Ermis M. Photo-crosslinked gelatin methacrylate hydrogels with mesenchymal stem cell and endothelial cell spheroids as soft tissue substitutes. J Mater Res. 2021; 36: 176–190. https://doi.org/10.1557/s43578-020-00091-4
[38] Liu J, Tan Y, Zhang H, Zhang Y, Xu P, Chen J, Poh YC, Tang K, Wang N, Huang B. Soft fibrin gels promote selection and growth of tumorigenic cells. Nat Mater. 2012; 11: 734–741. https://doi.org/10.1038/nmat3361
[39] Choi JY, Jang YS, Min SY, Song JY. Overexpression of MMP-9 and HIF-1α in breast cancer cells under hypoxic conditions. J Breast Cancer. 2011; 14: 88–95. https://doi.org/10.4048%2Fjbc.2011.14.2.88
[40] Kessenbrock K, Plaks V, Werb Z. Matrix metalloproteinases: Regulators of the tumor microenvironment. 2010; 141: 52–67. https://doi.org/10.1016/j.cell.2010.03.015
[41] Indelicato M, Pucci B, Schito L, Reali V, Aventaggiato M, Mazzarino MC, Stivala F, Fini M, Russo MA, Tafani M, Role of hypoxia and autophagy in MDA-MB-231 invasiveness. J Cell Physiol. 2010; 223: 359–368. https://doi.org/10.1002/jcp.22041
[42] Wicks EE, Semenza GL, Hypoxia-inducible factors: cancer progression and clinical translation. J Clin Investig. 2022; 132: e159839. https://doi.org/10.1172/JCI159839
[43] Däster S, Amatruda N, Calabrese D, Ivanek R, Turrini E, Droeser RA, Zajac P, Fimognari C, Spagnoli GC, Iezzi G, Mele V, Muraro MG. Induction of hypoxia and necrosis in multicellular tumor spheroids is associated with resistance to chemotherapy treatment. Oncotarget. 2017; 8: 1725–1736. https://doi.org/10.18632/oncotarget.13857
[44] Hagemann J, Jacobi C, Hahn M, Schmid V, Welz C, Schwenk-Zieger S, Stauber R, Baumeister P, Becker S. Spheroid-based 3D cell cultures enable personalized therapy testing and drug discovery in head and neck cancer. Anticancer Res. 2017; 37: 2201–2210. https://doi.org/10.21873/anticanres.11555
[45] Shi W, Kwon J, Huang Y, Tan J, Uhl CG, He R, Zhou C, Liu Y. Facile tumor spheroids formation in large quantity with controllable size and high uniformity. Sci Rep. 2018; 8: 6837. https://doi.org/10.1038/s41598-018-25203-3
[46] Yan L, Borregaard N, Kjeldsen L, Moses MA. The high molecular weight urinary matrix metalloproteinase (MMP) activity is a complex of gelatinase B/MMP-9 and neutrophil gelatinase-associated lipocalin (NGAL). Modulation of MMP-9 activity by NGAL. J Biol Chem. 2021; 276: 37258–37265. https://doi.org/10.1074/jbc.m106089200

Figures

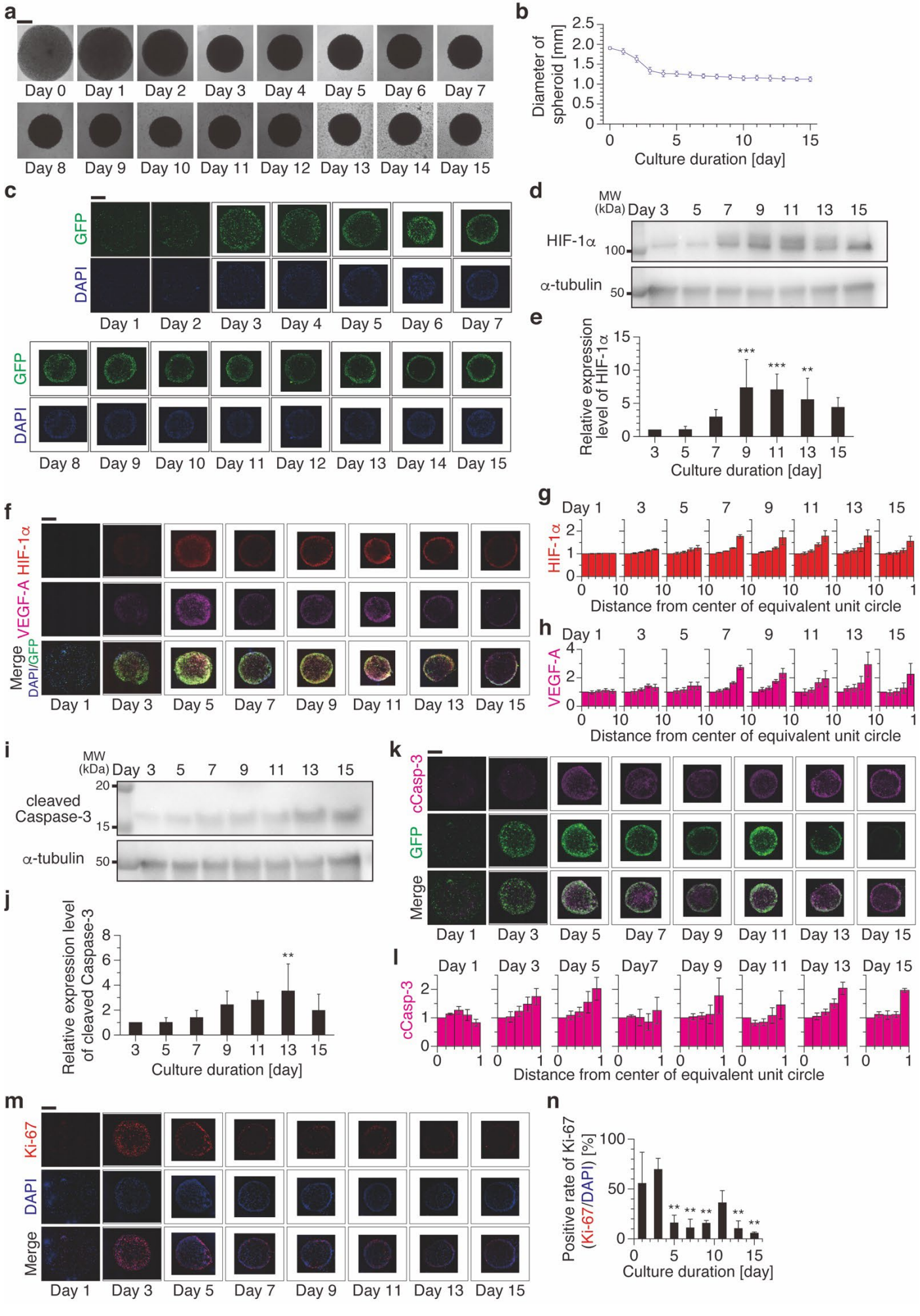
a
Day 0
Day 1
Day 2
Day 3
Day 4
Day 5
Day 6
Day 7
Day 8
Day 9
Day 10
Day 11
Day 12
Day 13
Day 14
Day 15
b
Diameter of spheroid [mm]
Culture duration [day]
c
GFP
DAPI
d
MW (kDa)
HIF-1α
α-tubulin
e
Relative expression level of HIF-1α
Culture duration [day]
f
HIF-1α
VEGF-A
Merge
DAPI/GFP
g
Distance from center of equivalent unit circle
h
VEGF-A
i
cleaved Caspase-3
α-tubulin
j
Relative expression level of cleaved Caspase-3
Culture duration [day]
k
cCasp-3
GFP
Merge
l
cCasp-3
Distance from center of equivalent unit circle
m
Ki-67
DAPI
Merge
n
Positive rate of Ki-67 (Ki-67/DAPI) [%]
Culture duration [day]

Fig. 1. MDA-MB-231 cell dynamics in the fast fabricated spheroid. (**a**) Time sequence phase-contrast images depicting spheroid contraction under the normoxic condition (21% O_2). Scale bar, 500 μm. (**b**) Spheroid diameter measured based on the phase-contrast images (mean ± SD, *n* = 5). (**c**) Quenching of GFP expressed in the cytoplasm of MDA-MB-231 cells in spheroids. Scale bar, 500 μm. (**d**) Representative blots of HIF-1α expressed in the MDA-MB-231 cells forming the spheroid. (**e**) Relative expression level of HIF-1α to that of α-tubulin after each culture duration, which was normalized by that on day 3 (mean + SD, *n* = 5). (**f**) Expression dynamics of HIF-1α and VEGF-A in MDA-MB-231 spheroids. Scale bar, 500 μm. Changes in the distribution of relative fluorescence intensity of (**g**) HIF-1α or (**h**) VEGF-A. Each data was normalized by the intensity in the 20% region from the center (mean ± SD, *n* = 3). (**i**) Representative blots of cleaved Caspase-3 expressed in the MDA-MB-231 cells forming the spheroid. (**j**) Caspase-3 activation in the spheroid, expressed as the relative intensity of cleaved Caspase-3 to that of α-tubulin. The values are normalized by that on day 3 (mean + SD, *n* = 5). (**k**) Activation dynamics of Caspase-3 (cCasp-3) in MDA-MB-231 spheroids. Scale bar, 500 μm. (**l**) Changes in the distribution of relative fluorescence intensity of cleaved Caspase-3 (cCasp-3). Each data was normalized by the intensity in the 20% region from the center (mean ± SD, *n* = 3). (**m**) Distribution of Ki-67 positive cells in the spheroid at each number of culture days. Scale bar, 500 μm. (**n**) Change in positive rate of Ki-67 with culture duration calculated from fluorescent images of frozen sections (mean + SD, *n* = 3). ** $p < 0.05$, *** $p < 0.01$ *vs.* the expression levels on day 3 (Dunnett's test; **e**, **j**) or the positive rate on day 1 (Dunnett's test; **n**).

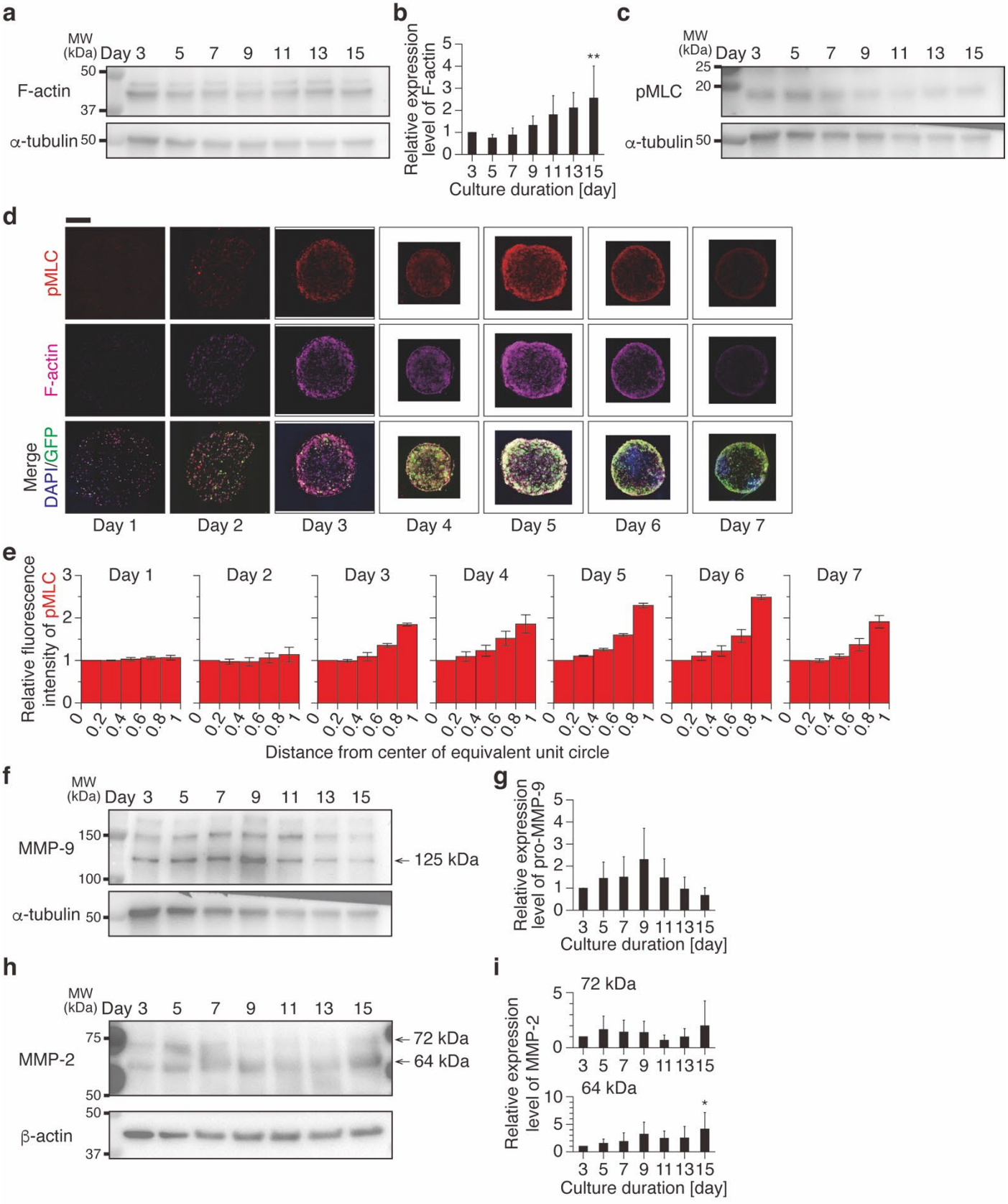
a
MW (kDa)
Day 3 5 7 9 11 13 15
50
F-actin
37
α-tubulin 50
b
Relative expression level of F-actin
**
Culture duration [day]
c
MW (kDa)
Day 3 5 7 9 11 13 15
25
20
pMLC
α-tubulin 50
d
pMLC
F-actin
Merge DAPI/GFP
Day 1 Day 2 Day 3 Day 4 Day 5 Day 6 Day 7
e
Relative fluorescence intensity of pMLC
Day 1 Day 2 Day 3 Day 4 Day 5 Day 6 Day 7
Distance from center of equivalent unit circle
f
MW (kDa)
Day 3 5 7 9 11 13 15
MMP-9
150
100
← 125 kDa
α-tubulin 50
g
Relative expression level of pro-MMP-9
Culture duration [day]
h
MW (kDa)
Day 3 5 7 9 11 13 15
MMP-2
75
50
← 72 kDa
← 64 kDa
50
β-actin
37
i
Relative expression level of MMP-2
72 kDa
64 kDa
*
Culture duration [day]
j
DMSO
BLB
Day 0 Day 1 Day 2 Day 3 Day 4 Day 5 Day 6 Day 7
k
DMSO (0.1%)
BLB (5 μM)
Diameter of spheroid [mm]
Ratio of change in spheroid diameter
***
Culture duration [day]

Fig. 2. Actomyosin systems play a critical role for contractility of the MDA-MB-231 spheroid. (**a**–**g**) Expression of proteins, which are related to the spheroid contraction, in the MDA-MB-231 cells. (**a**) Representative blots of F-actin expressed in the MDA-MB-231 cells forming the spheroid. (**b**) Relative expression level of F-actin to that of α-tubulin after each culture duration, which was normalized by that on day 3 (mean + SD, $n = 5$). (**c**) Activation of actomyosin contractility in the spheroid, expressed as phosphorylation of myosin light chain 2 (pMLC). (**d**) Localization of phosphorylation of MLC in MDA-MB-231 spheroids. Scale bar, 500 μm. (**e**) Changes in the distribution of relative fluorescence intensity of pMLC. Each data was normalized by the intensity in the 20% region from the center (mean ± SD, $n = 3$). (**f**) Representative blots of MMP-9 expressed in the MDA-MB-231 cells forming the spheroid. MMP-9 appeared to form a complex with neutrophil gelatinase-associated lipocalin (NGAL), showing a high intensity band with a molecular weight of 125 kDa [46]. (**g**) Relative expression level of MMP-9 to that of α-tubulin after each culture duration, which was normalized by that on day 3 (mean + SD, $n = 5$). (**h**) Representative blots of MMP-2 expressed in the MDA-MB-231 cells forming the spheroid. Two bands indicate the proenzyme form (72 kDa) and the active form (64 kDa), respectively. (**i**) Relative expression levels of pro- and active MMP-2 to that of β-actin each culture duration, which were normalized by that on day 3 (mean + SD, $n = 5$). (**j**) Time sequence phase-contrast images depicting spheroid contraction under the condition of myosin inhibition with blebbistatin (BLB). Scale bar, 500 μm. (**k**) Quantitative evaluation of spheroid diameter based on the phase-contrast images and the calculated change ratio of spheroid diameter by the original value over time (mean ± SD, $n = 5$). * $p < 0.1$, ** $p < 0.05$ vs. expression levels on day 3 (Dunnett's test; **b**, **e**, **g**). ** $p < 0.01$ (Welch's *t*-test; **k**).

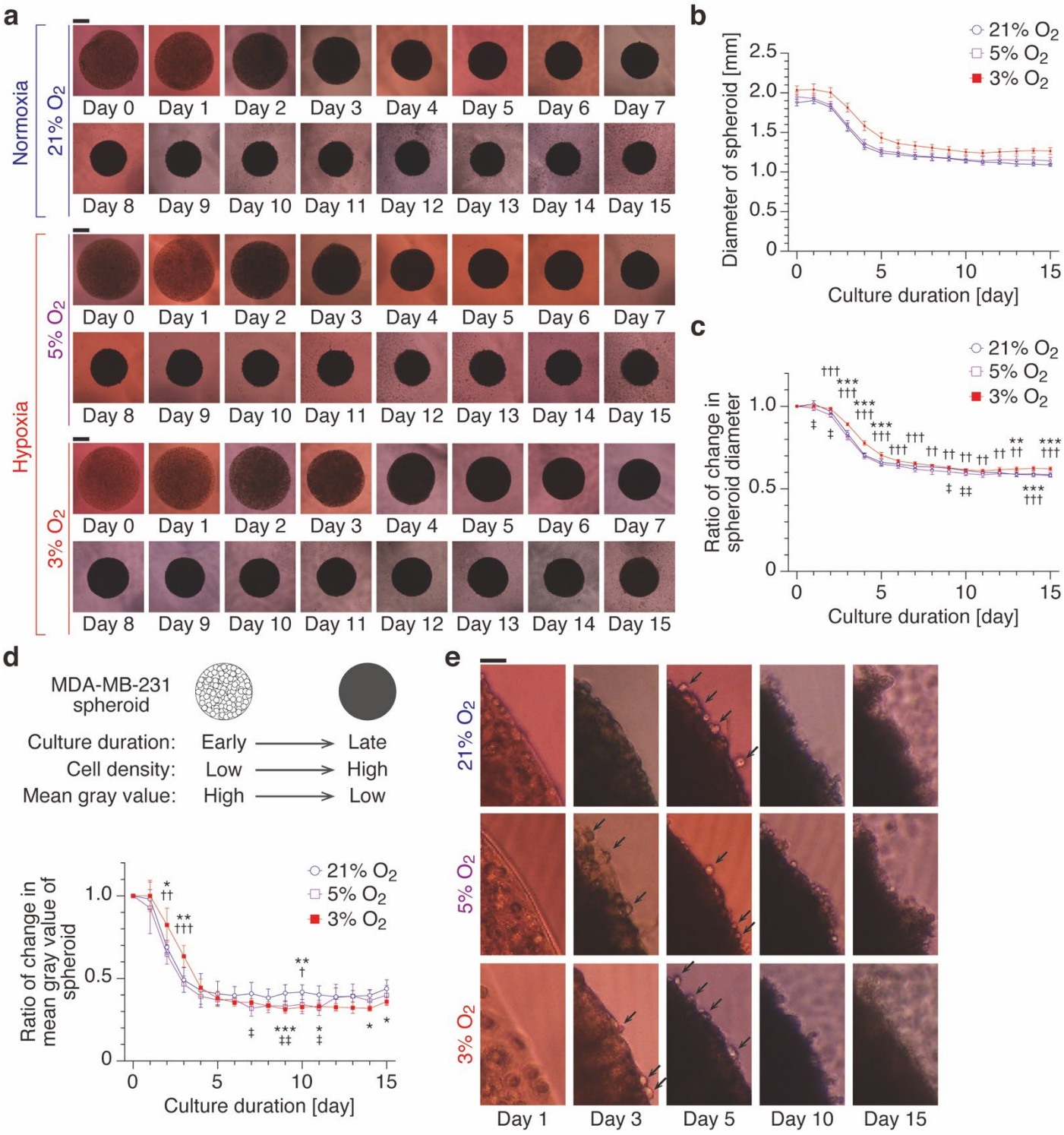

Fig. 3. Highly hypoxic conditions caused a delay in the MDA-MB-231 spheroid contraction. (**a**) MDA-MB-231 spheroid contraction under hypoxic conditions for 15 days. Scale bars, 500 μm. (**b**) Spheroid diameter measured with the phase-contrast images under each oxygen condition (mean ± SD, *n* = 5). (**c**) Change ratio of spheroid diameter against the original value (mean ± SD, *n* = 5). (**d**) Quantification of cell density in the spheroid under each oxygen condition based on transmitted light intensity (mean ± SD, *n* = 5). (**e**) Representative situation of the MDA-MB-231 cells escaping from their spheroid (black arrows). The more cells escaped, the rougher the spheroid surface becomes (after day10). Scale bar; 50 μm. * $p < 0.1$, ** $p < 0.05$, ** $p < 0.01$ (3%

O_2 vs. 21% O_2); †† $p < 0.05$, ††† $p < 0.01$ (3% O_2 vs. 5% O_2); ‡ $p < 0.1$, ‡‡ $p < 0.05$ (5% O_2 vs. 21% O_2), (Tukey-Kramer test; **c**, **d**).

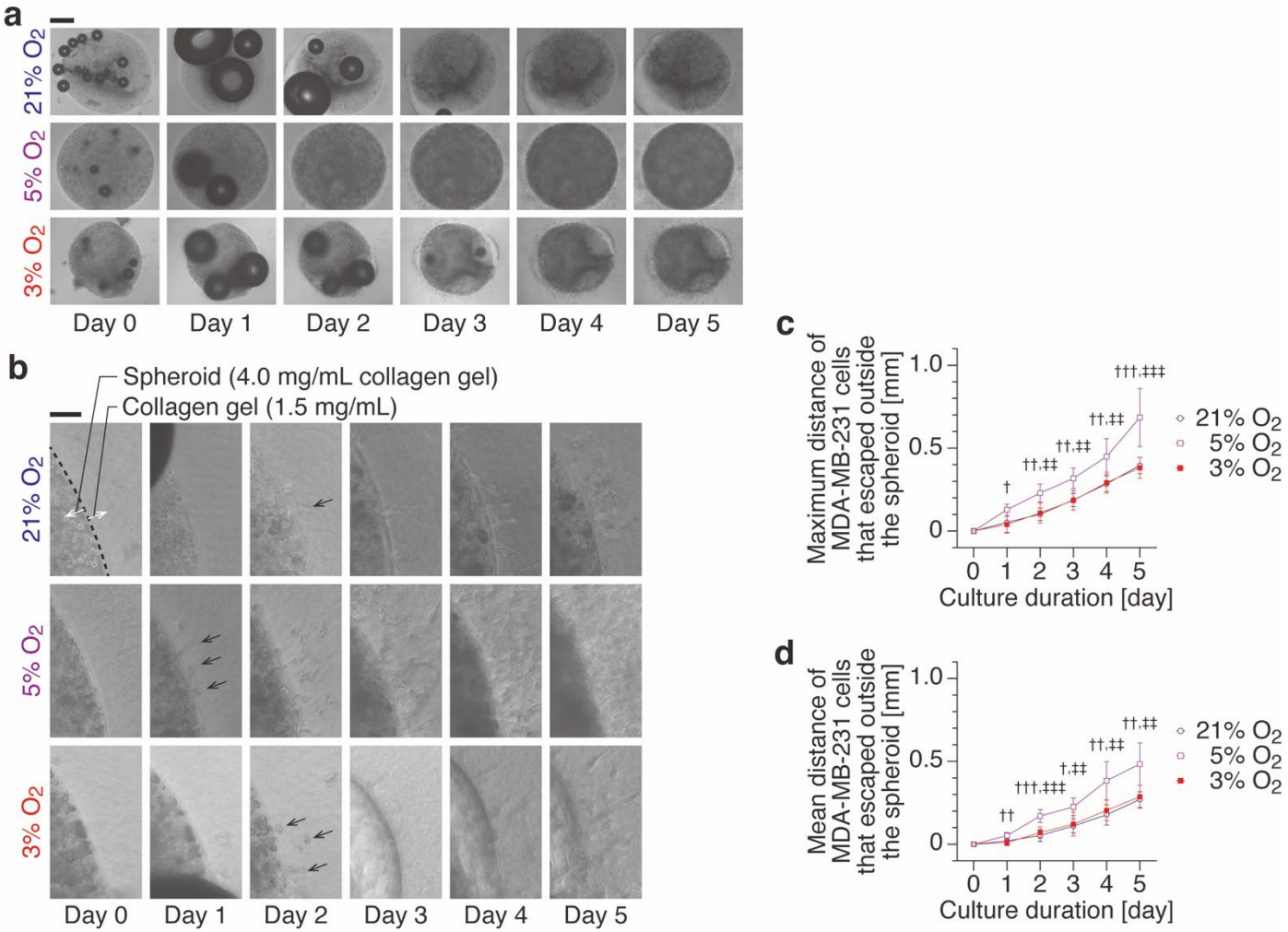

Fig. 4. Delayed contraction of MDA-MB-231 spheroids under the highly hypoxic condition is independent of the escape of cells from the spheroid. (**a**) Time sequence phase-contrast images depicting spheroids embedded in collagen gel adjusted to 1.5 mg/mL under each oxygen condition. Scale bar, 500 μm. (**b**) Magnified images around the boundary between the spheroid and the surrounding collagen gel. Black arrows indicate the first observation of the cells that escaped and migrated into the surrounding collagen gel. Scale bar, 50 μm. (**c**, **d**) Quantitative evaluation of the distance that MDA-MB-231 cells escaped from the spheroid into the surrounding gel based on the phase-contrast images (mean ± SD, $n = 5$). † $p < 0.1$, †† $p < 0.05$, ††† $p < 0.01$ (3% O_2 vs. 5% O_2); ‡ $p < 0.05$, ‡‡ $p < 0.01$, (5% O_2 vs. 21% O_2), (Tukey-Kramer test; **c**, **d**).

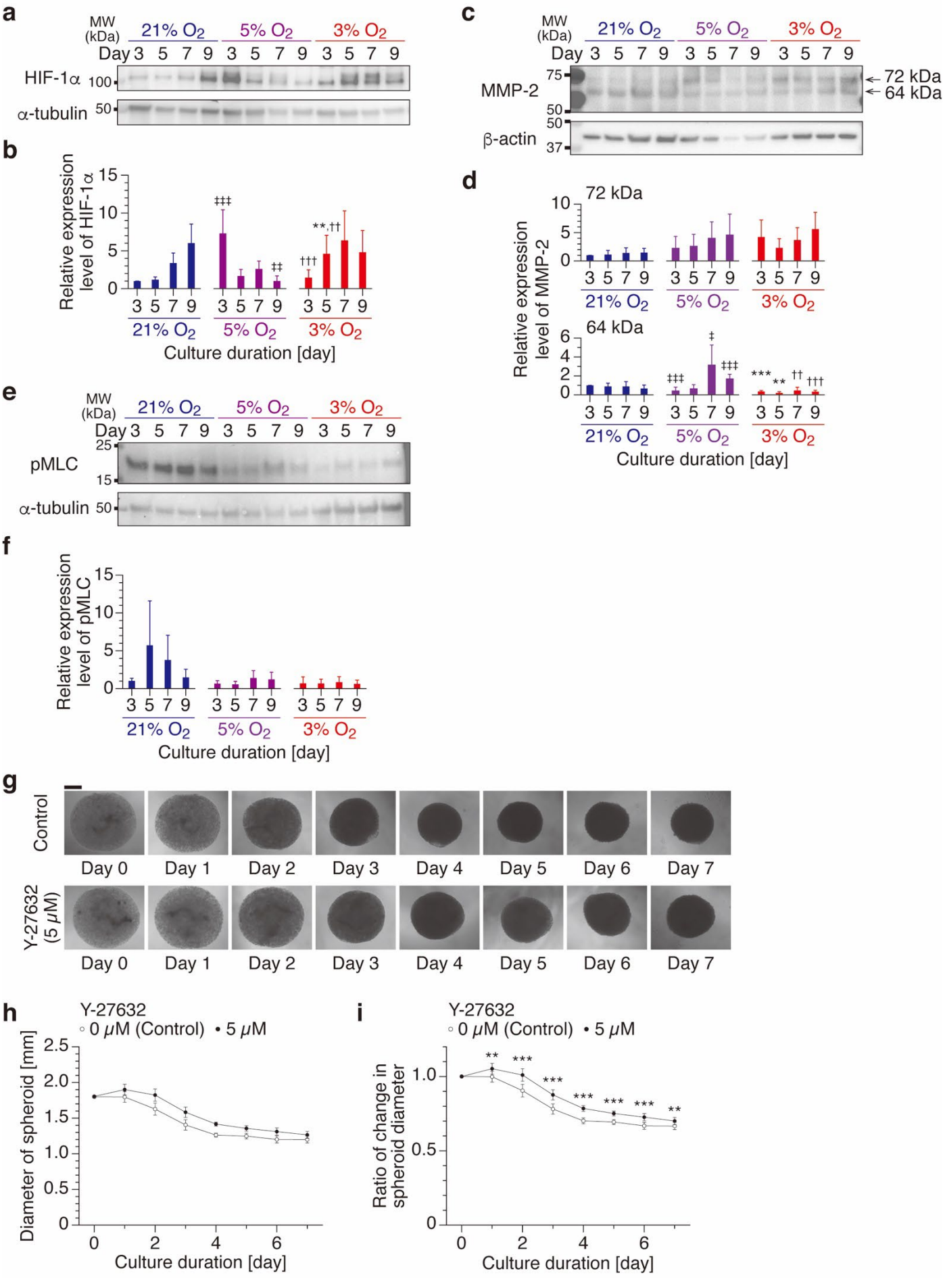
a
MW (kDa)
21% O2
5% O2
3% O2
Day 3 5 7 9 3 5 7 9 3 5 7 9
HIF-1α 100
α-tubulin 50
b
Relative expression level of HIF-1α
Culture duration [day]
c
MMP-2 75 50
β-actin 50 37
72 kDa
64 kDa
d
72 kDa
64 kDa
Relative expression level of MMP-2
Culture duration [day]
e
pMLC 25 15
α-tubulin 50
f
Relative expression level of pMLC
Culture duration [day]
g
Control
Y-27632 (5 μM)
Day 0 Day 1 Day 2 Day 3 Day 4 Day 5 Day 6 Day 7
h
Y-27632
○ 0 μM (Control) • 5 μM
Diameter of spheroid [mm]
Culture duration [day]
i
Y-27632
○ 0 μM (Control) • 5 μM
Ratio of change in spheroid diameter
Culture duration [day]

Fig. 5. The function of Rho-associated protein kinase (ROCK) is associated with a delay in the contraction of MDA-MB-231 spheroids under highly hypoxic conditions. (**a**–**f**) Expression of proteins, which are related to the spheroid contraction under hypoxic conditions, in the MDA-MB-231 cells. (**a**) Representative blots of HIF-1α expressed in the MDA-MB-231 cells forming the spheroids. (**b**) Relative expression level of HIF-1α to that of α-tubulin after each culture duration, which was normalized by that on day 3 under the normoxic condition (mean + SD, n = 5). (**c**) Representative blots of MMP-2 expressed in the MDA-MB-231 cells. (**d**) Relative expression levels of pro- and active MMP-2 to that of β-actin after each culture duration, which were normalized by those on day 3 under the normoxic condition (mean + SD, n = 5). (**e**) Representative blots of pMLC in the MDA-MB-231 cells. (**f**) Activation of actomyosin contractility in the spheroid, indicated by relative expression level of pMLC to that of α-tubulin after each culture duration, which was normalized by that under the normoxic condition on day 3 (mean + SD, n = 5). (**g**) Time sequence phase-contrast images showing spheroid contraction under the condition of ROCK1/2 inhibition with Y-27632. Scale bar, 500 μm. (**h**) Quantitative evaluation of spheroid diameter based on the phase-contrast images and (**i**) the calculated change ratio of spheroid diameter against the original value over time (mean ± SD, n = 5). ** $p < 0.05$, *** $p < 0.01$ (3% O_2 vs. 21% O_2); †† $p < 0.05$, ††† $p < 0.01$ (3% O_2 vs. 5% O_2); ‡ $p < 0.1$, ‡‡ $p < 0.05$, ‡‡‡ $p < 0.01$ (5% O_2 vs. 21% O_2), (Tukey-Kramer test; **b**, **d**, **f**). ** $p < 0.05$, *** $p < 0.01$ (Welch's t-test; **i**).

Supplementary Information

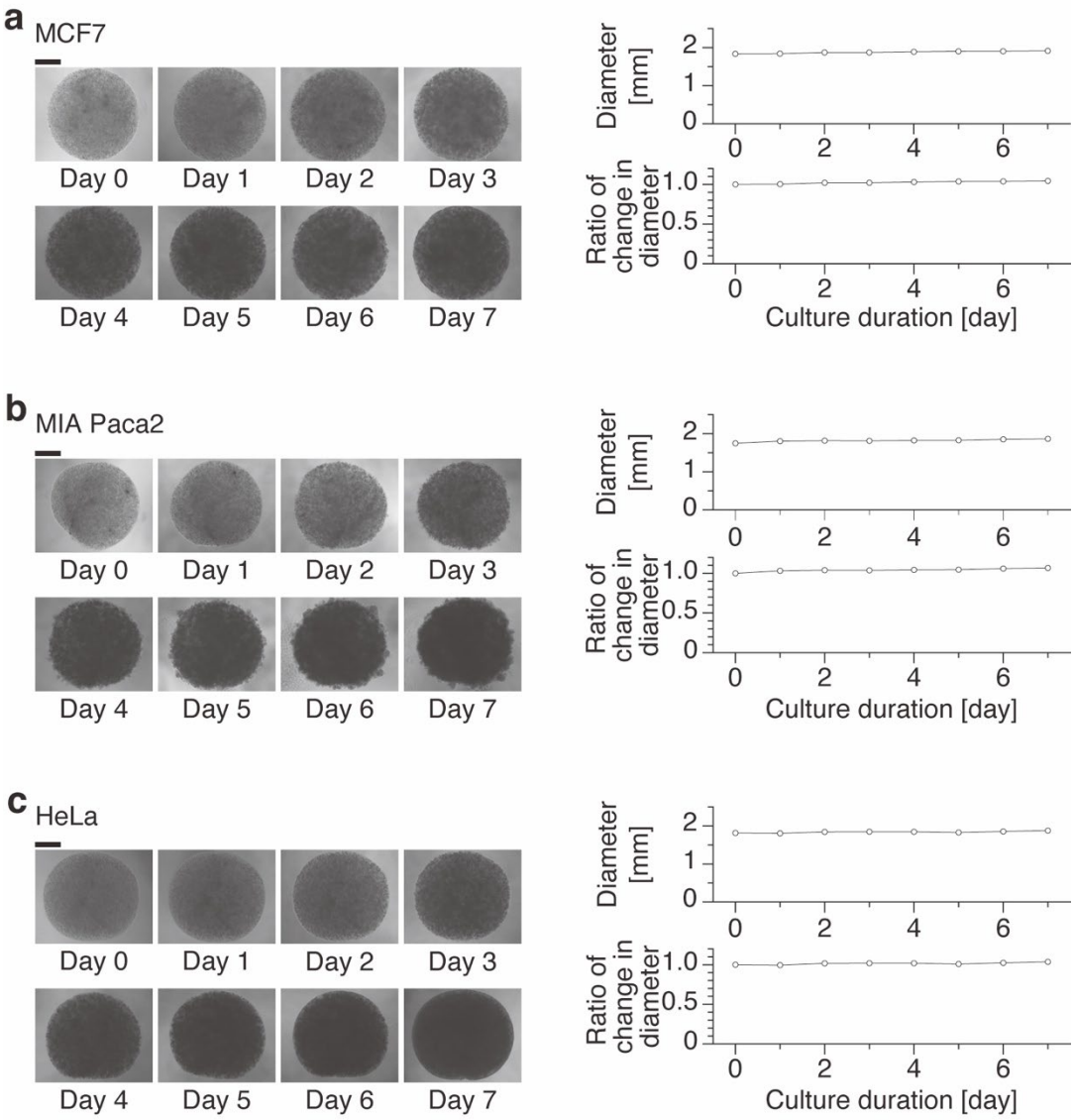

Supplementary Fig. 1. Spheroids of different types of cancer cell lines formed by the fast fabrication method. Time sequence phase-contrast images showing (**a**) MCF7, (**b**) MIA PaCa-2, or (**c**) HeLa, and quantitative evaluation of spheroid diameter based on the phase-contrast images and the calculated change ratio of spheroid diameter by the original value over time (mean ± SD, *n* = 5). Scale bar, 500 μm.

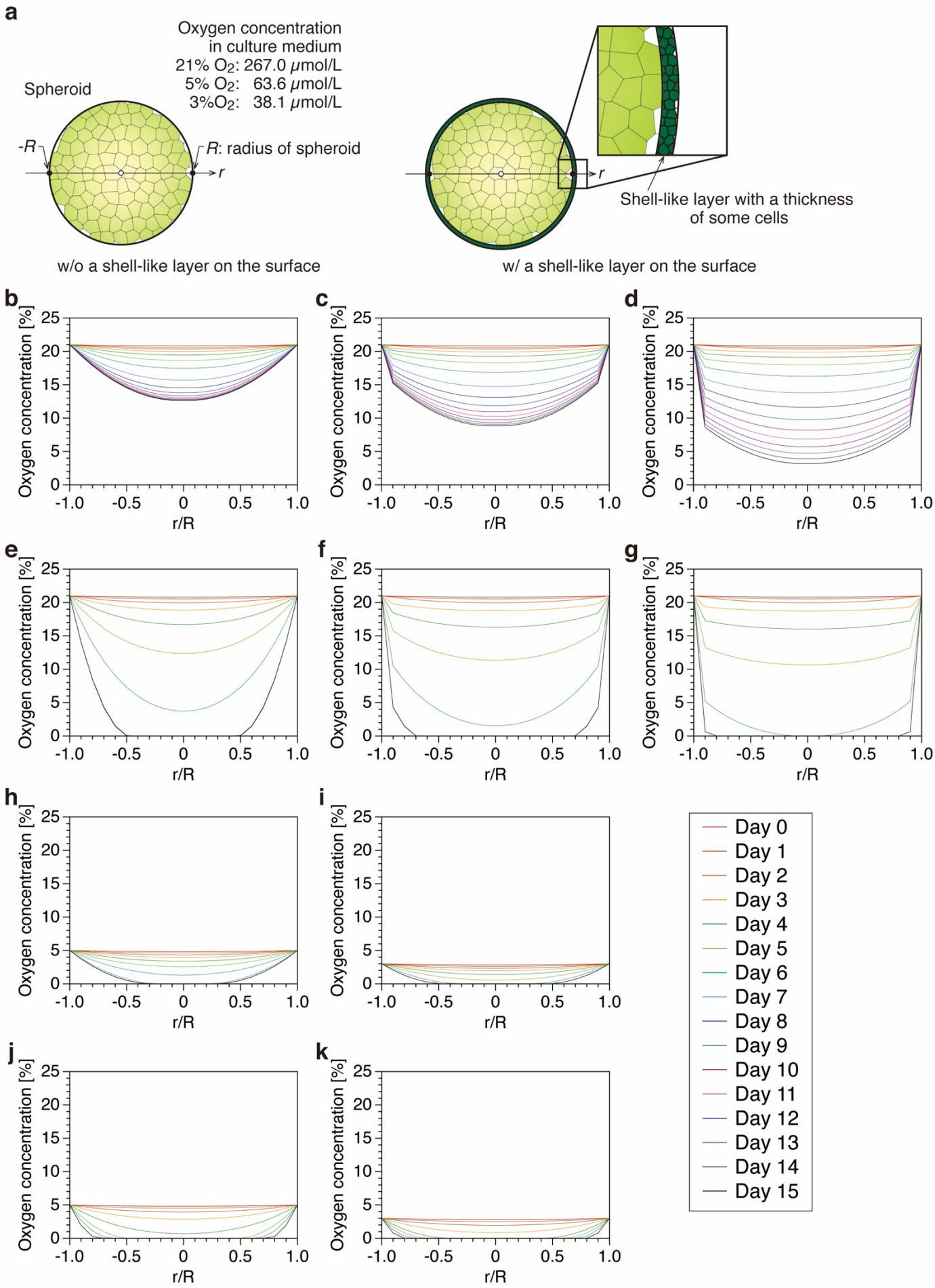
a
Oxygen concentration
in culture medium
21% O2: 267.0 μmol/L
5% O2: 63.6 μmol/L
3%O2: 38.1 μmol/L
Spheroid
-R
R: radius of spheroid
r
w/o a shell-like layer on the surface
r
Shell-like layer with a thickness
of some cells
w/ a shell-like layer on the surface
b
c
d
e
f
g
h
i
j
k
Oxygen concentration [%]
r/R
Day 0
Day 1
Day 2
Day 3
Day 4
Day 5
Day 6
Day 7
Day 8
Day 9
Day 10
Day 11
Day 12
Day 13
Day 14
Day 15

Supplementary Fig. 2. Estimated changes in oxygen concentration in spheroids. (**a**) The mathematical model used to calculate oxygen diffusion and consumption. (**b**–**d**) Variation of oxygen concentration for each day when the number of cells increased 1.5-fold in one day; **b**, without the shell-like layer; **c**, the oxygen permeability of the shell-like layer was set to 1/4 of the level of the case without the shell-like layer; **d**, its permeability was set to 1/10 of the level in the absence of the shell-like layer. (**e**–**g**) Variation of oxygen concentration for each day when the number of cells doubled in one day; **e**, without the shell-like layer; **f**, the oxygen permeability of the shell-like layer was set to 1/4 of that of the case without the shell-like layer; **g**, its permeability was set to 1/10 of that of the case without the shell-like layer. (**h–k**) Oxygen concentration in the spheroids without shell-like layer under different oxygen conditions; **h**, **i**, when cells were 1.5 times larger in one day under (**h**) 5% O_2 and (**i**) 3% O_2; **j**, **k**, when cells were two times larger in one day under (**j**) 5% O_2 and (**k**) 3% O_2.

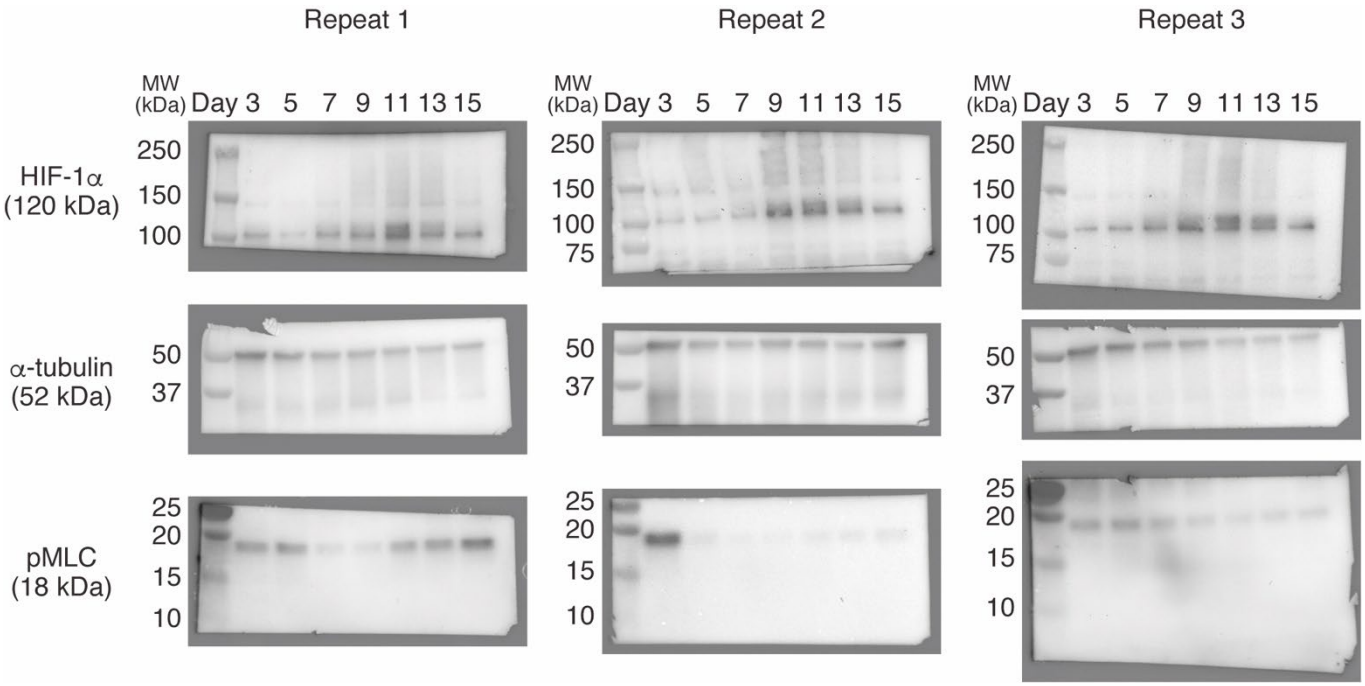

Supplementary Fig. 3. Original western blot of pMLC for three repeats. Whole membrane was cut to blot for HIF-1α and α-tubulin simultaneously with pMLC.

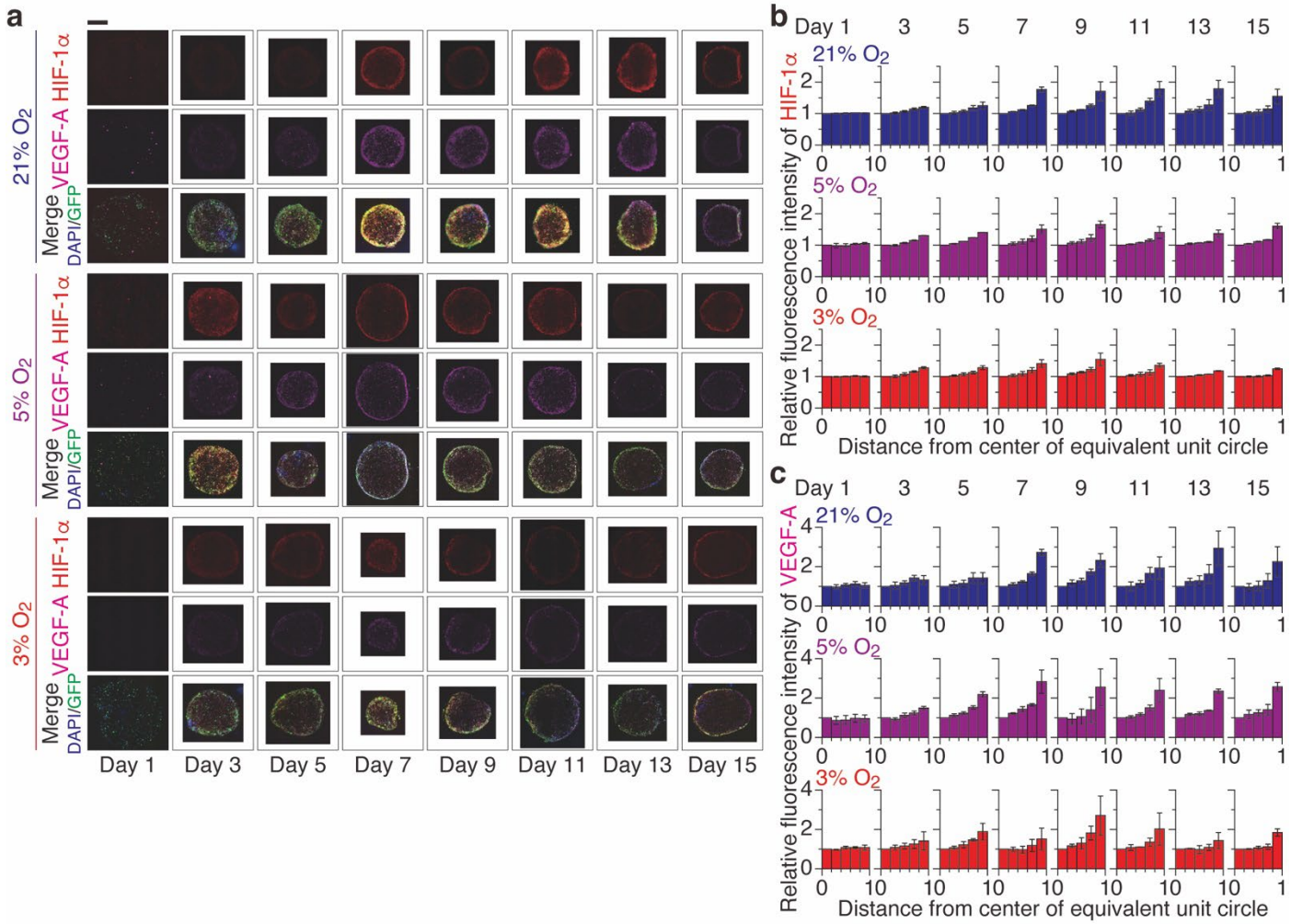

Supplementary Fig. 4. Expression dynamics of HIF-1α and VEGF-A in MDA-MB-231 spheroids under each oxygen concentration. (**a**) Representative fluorescence images of HIF-1α and VEGF-A in MDA-MB-231 spheroids. Scale bar, 500 μm. Changes in the distribution of relative fluorescence intensity of (**b**) HIF-1α or (**c**) VEGF-A. Each data was normalized by the intensity in the 20% region from the center (mean ± SD, *n* = 3).

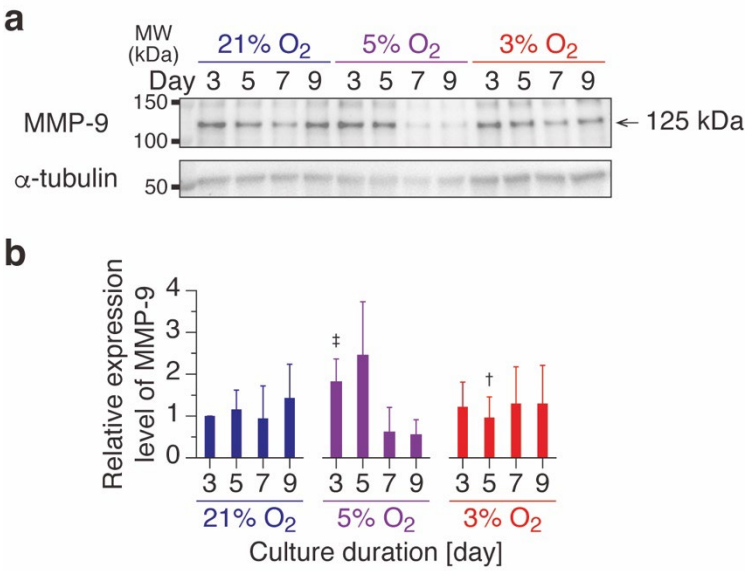

Supplementary Fig. 5. Expression of MMP-9 enzyme proteins in the MDA-MB-231 spheroid exposed to hypoxic conditions. (**a**) Representative blots of MMP-9 expressed in the MDA-MB-231 cells forming the spheroids. MMP-9 appeared to form a complex with neutrophil gelatinase-associated lipocalin (NGAL), showing a high intensity band with a molecular weight of 125 kDa. (**b**) Relative expression level of MMP-9 to that of α-tubulin after each culture duration, which was normalized by that under the normoxic condition on day 3 (mean + SD, $n = 5$). $^{\dagger}p < 0.1$ (3% O_2 vs. 5% O_2); $^{\ddagger}p < 0.1$ (5% O_2 vs. 21% O_2), (Tukey-Kramer test; **b**).

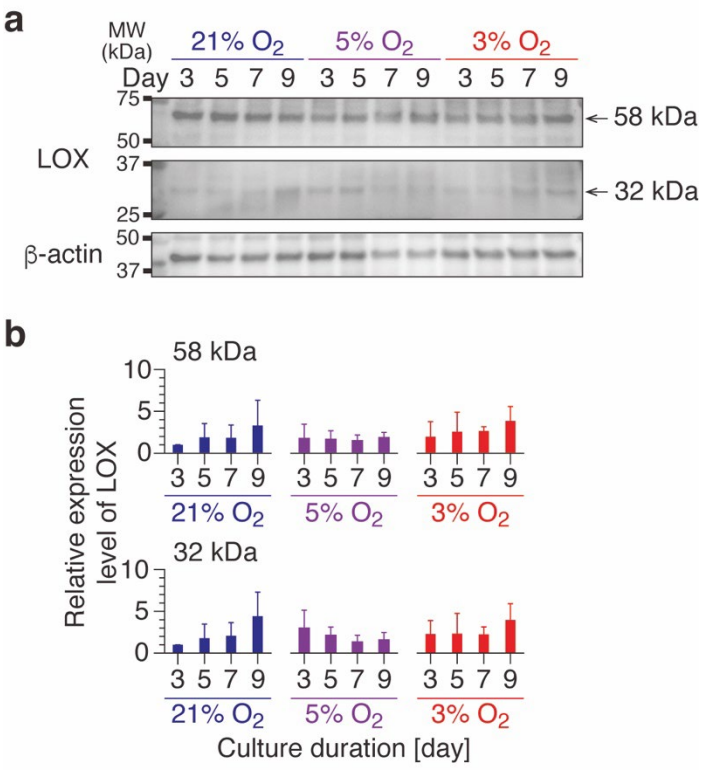

Supplementary Fig. 6. Expression of lysyl oxidase (LOX), which is important for the formation of the extracellular matrix, in the MDA-MB-231 spheroid exposed to hypoxic conditions. (**a**) Representative blots of LOX expressed in the MDA-MB-231 cells. Two bands indicate the glycosylated form (58 kDa) and the mature form (32 kDa), respectively. (**b**) Relative expression levels of glycosylated and mature LOX to that of β-actin after each culture duration, which were normalized by those under the normoxic condition on day 3 (mean + SD, *n* = 5, Tukey-Kramer test; **b**).

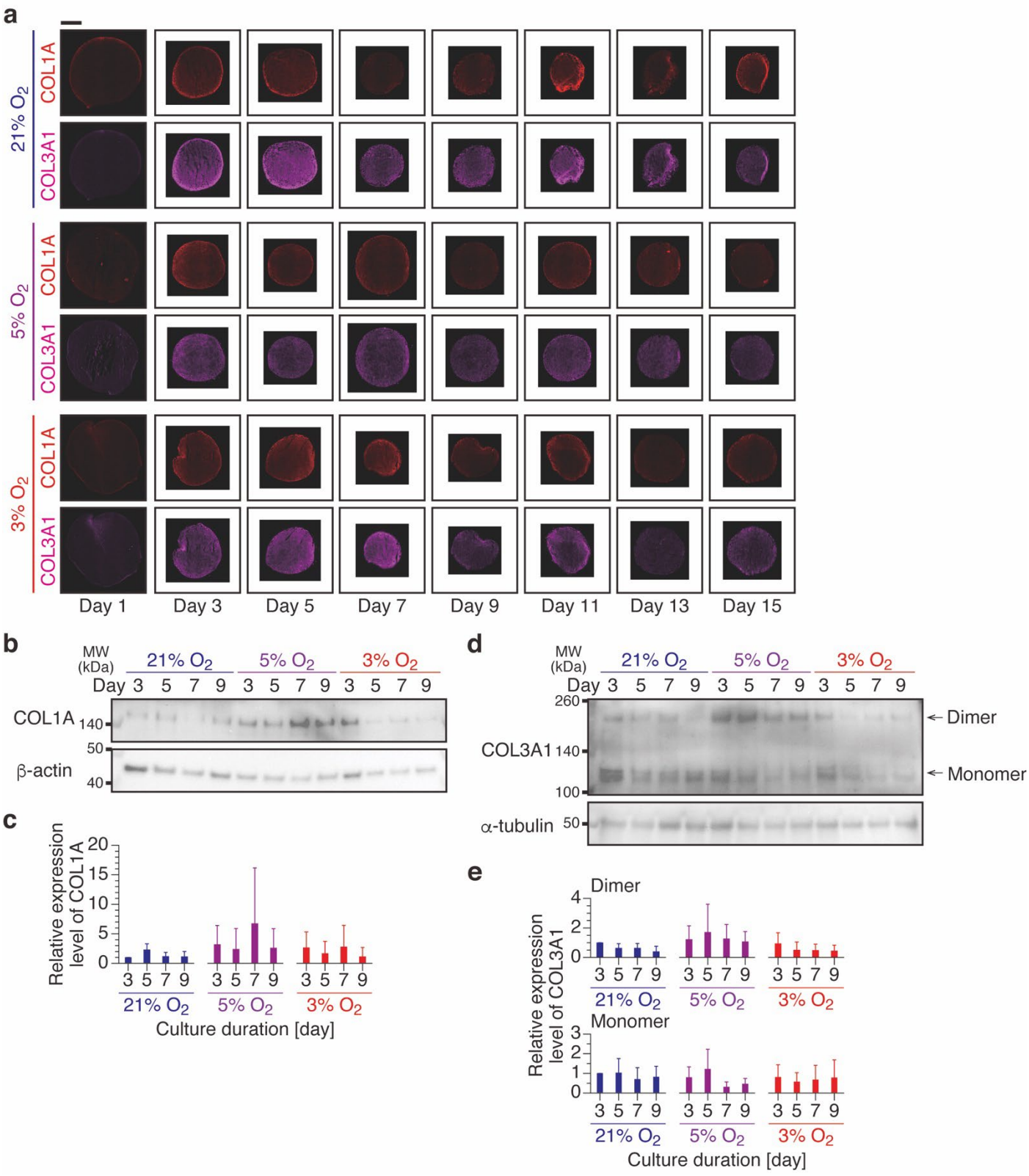

Supplementary Fig. 7. Expression dynamics of collagen type 1 (COL1A) and type 3 (COL3A1) in the MDA-MB-231 spheroid exposed to each oxygen condition. (**a**) Representative fluorescence images of COL1A and COL3A1 in MDA-MB-231 spheroids (*n* = 3). Scale bar, 500 μm. (**b**) Representative blots of COL1A expressed in the MDA-MB-231 cells. (**c**) Relative expression levels of COL1A to that of β-actin after each culture duration, which were normalized by those under the normoxic condition on day 3 (mean + SD, *n* = 5) (**d**) Representative blots of COL3A1 expressed in the MDA-MB-231 cells. Two bands indicate the monomer form and

the dimer form, respectively. (**e**) Relative expression levels of monomer- and dimer- COL3A1 to that of α-tubulin after each culture duration, which were normalized by those under the normoxic condition on day 3 (mean + SD, *n* = 5). There were no significant differences between the data (Tukey-Kramer test; **c**, **e**).

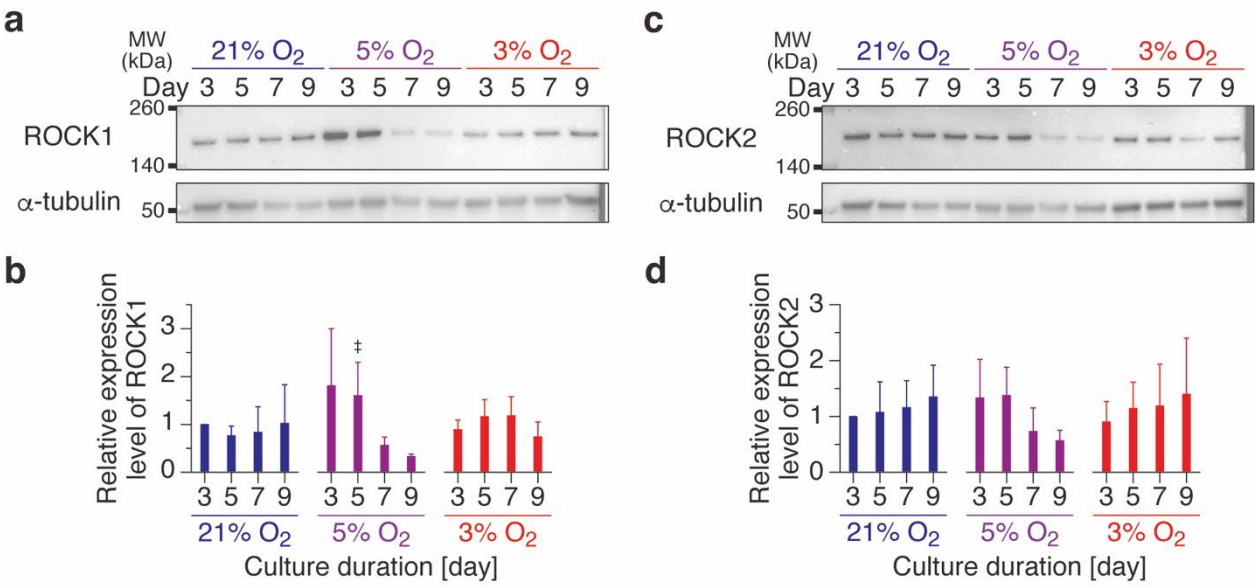

Supplementary Fig. 8. Expression of Rho-associated protein kinase 1/2 (ROCK1/2), which is a key regulator of actin organization, in the MDA-MB-231 spheroid exposed to hypoxic conditions. (**a**) Representative blots of ROCK1 expressed in the MDA-MB-231 cells. (**b**) Relative expression levels of ROCK1 to that of α-tubulin after each culture duration, which were normalized by that under the normoxic condition on day 3 (mean + SD, *n* = 5). (**c**) Representative blots of ROCK2 expressed in the MDA-MB-231 cells. (**b**) Relative expression levels of ROCK2 to that of α-tubulin after each culture duration, which were normalized by that under the normoxic condition on day 3 (mean + SD, *n* = 5). Tukey-Kramer test; **b**). ‡ $p < 0.1$ (5% O_2 vs. 21% O_2), (Tukey-Kramer test; **b**, **c**).

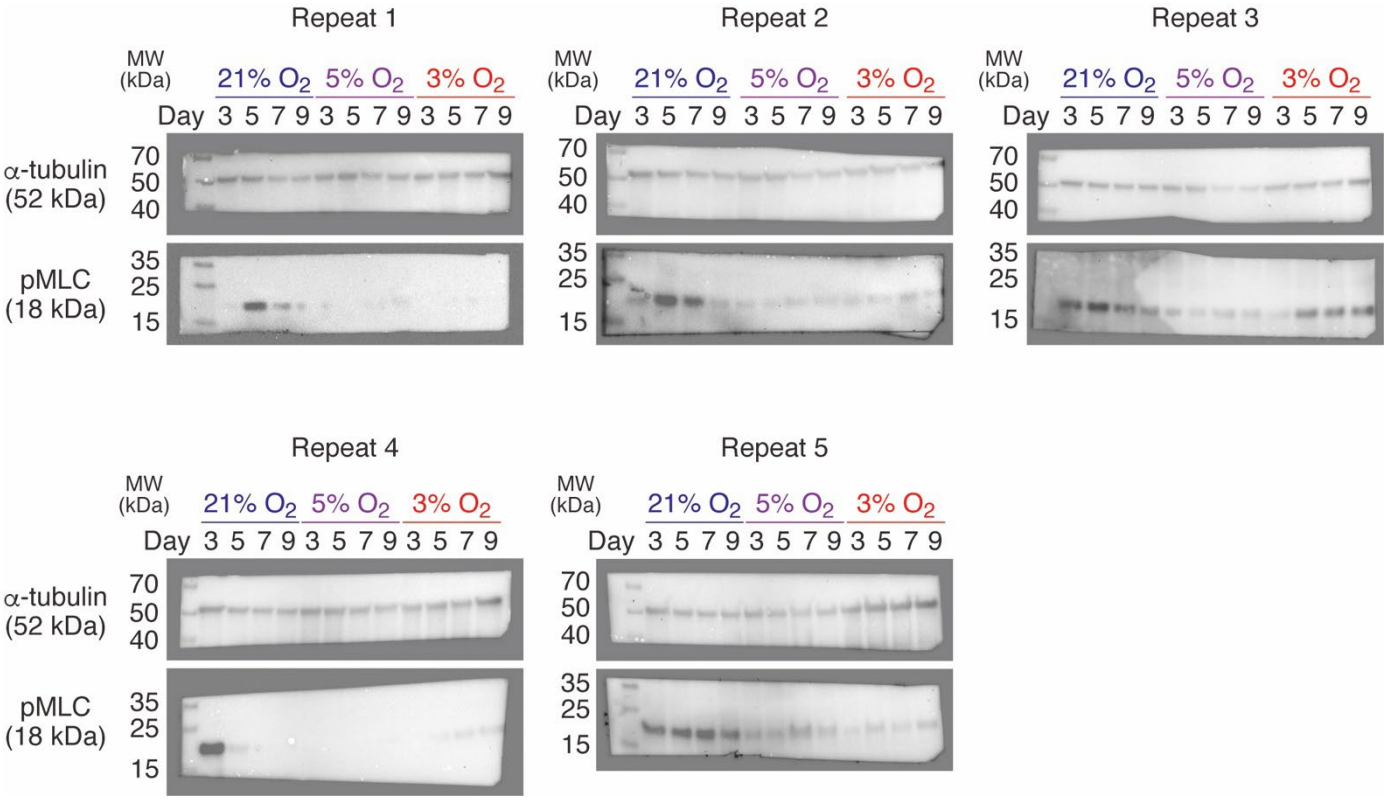

Supplementary Fig. 9. Original western blot of pMLC under three oxygen conditions for five repeats. Whole membrane was cut to blot for α-tubulin simultaneously with pMLC.

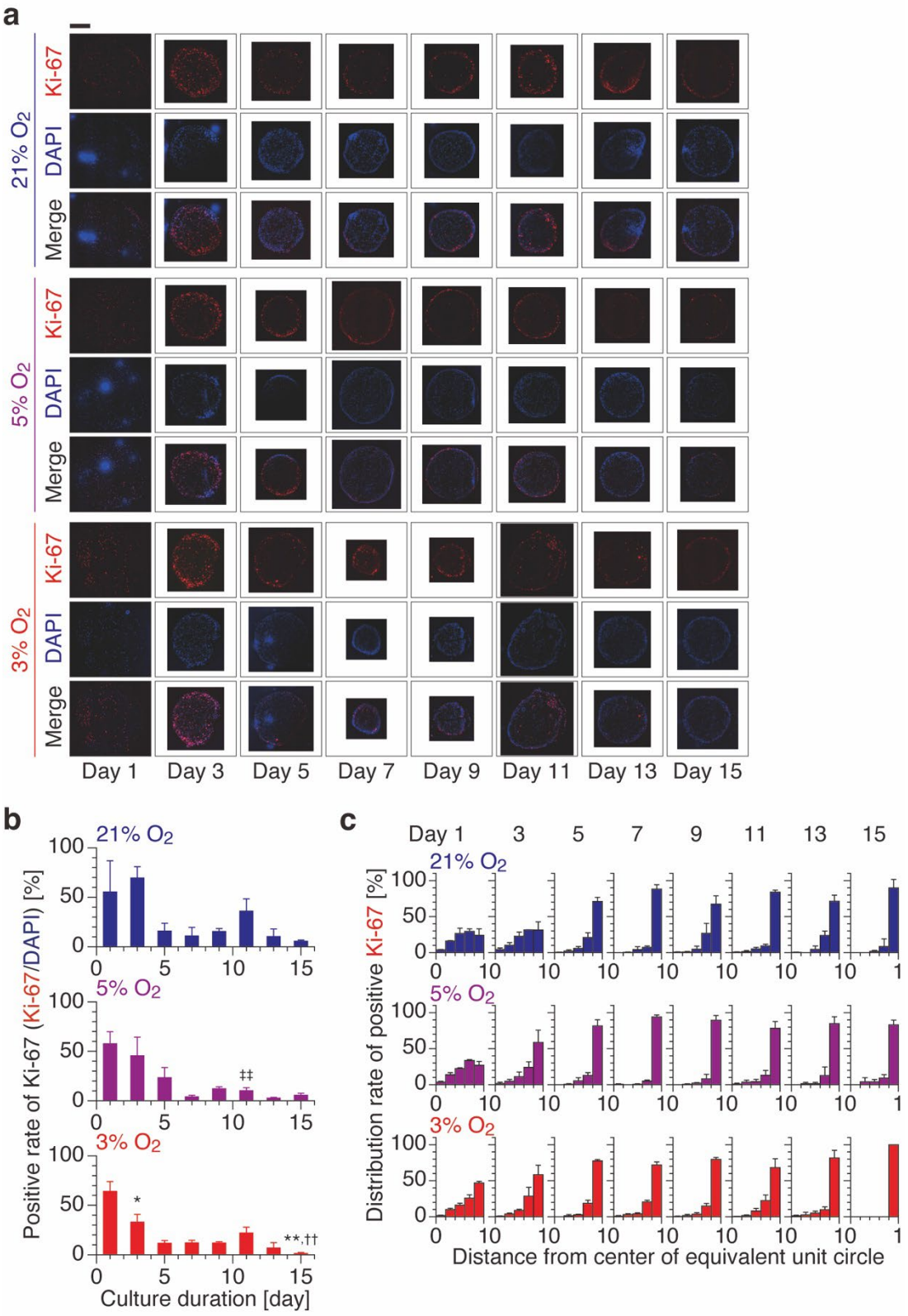

Supplementary Fig. 10. Distribution of Ki-67 positive cells in the spheroid at each number of culture days. (a) Representative fluorescence images of Ki-67 in MDA-MB-231 spheroids. Scale bar, 500 μm. (**b**) Change in positive rate of Ki-67 with culture duration calculated from fluorescent images of frozen sections (mean + SD, *n* = 3). (**c**) Changes in the distribution rate of Ki-67 positive cells. Each data was normalized by the intensity in the 20% region from the center (mean + SD, *n* = 3). * $p < 0.1$, ** $p < 0.05$ (3% O_2 vs. 21% O_2); †† $p < 0.05$ (3% O_2 vs. 5% O_2); ‡‡ $p < 0.05$ (5% O_2 vs. 21% O_2), (Tukey-Kramer test; **b**).

Supplementary Table 1.

List of primary antibodies used in this study.

Substance	Host species	Supplier	Catalog #	Dilution (Application)
Anti-HIF-1α	Rabbit	Cell Signaling Technology	36169	1:5000 (WB)
Anti-HIF-1α	Mouse	Cell Signaling Technology	79233	1:500 (IF)
Anti-VEGF-A	Rabbit	Cell Signaling Technology	50661	1:100 (IF)
Anti-Cleaved-Caspase 3	Rabbit	Proteintech	25546-1-AP	1:2000 (WB) 1:100 (IF)
Anti-F-Actin	Mouse	Abcam	ab305	1:2000 (WB)
Anti-phospho-myosin light chain 2 (Thr18/Ser19)	Rabbit	Cell Signaling Technology	3674	1:1000 (WB) 1:100 (IF)
Anti-Ki-67	Mouse	Cell Signaling Technology	9499	1:500 (IF)
Anti-MMP-9	Rabbit	Cell Signaling Technology	13667	1:1000 (WB)
Anti-MMP-2	Rabbit	Cell Signaling Technology	40994	1:1000 (WB)
Anti-LOX	Rabbit	Novus Biologicals	NB100-2527	1:1000 (WB)
Anti-COL1A	Mouse	Santa Cruz Biotechnology	sc-59772	1:1000 (WB) 1:100 (IF)
Anti-Collagen Type III (COL3A1)	Rabbit	Proteintech	22734-1AP	1:1000 (WB) 1:100 (IF)
Anti-alpha Tubulin	Rabbit	Cell Signaling Technology	2125	1:5000 (WB)
Anti-beta-Actin	Mouse	Santa Cruz Biotechnology	sc-47778	1:5000 (WB)

Supplementary Table 2.

List of secondary antibodies used in this study.

Substance	Conjugated label	Supplier	Catalog #	Dilution (Application)
Anti-mouse IgG	HRP	Cell Signaling Technology	7076	1:5000 (WB)
Anti-rabbit IgG	HRP	Cell Signaling Technology	7074	1:5000 (WB)
Anti-mouse IgG	Alexa Fluor 555	Thermo Fisher Scientific	A21422	1:200 (IF)
Anti-rabbit IgG	Alexa Fluor 555	Thermo Fisher Scientific	A21429	1:200 (IF)
Anti-rabbit IgG	Alexa Fluor Plus 647	Thermo Fisher Scientific	A32733	1:200 (IF)

Supplementary Source Code 1.

Program to extract pixel-by-pixel coordinates and fluorescence intensity values of regions of interest.

****

```
import ij.*;
import ij.process.*;
import ij.gui.*;
import ij.gui.FreehandRoi.*;
import ij.gui.Roi.*;
import ij.measure.Measurements.*;
import java.awt.*;
import java.awt.image.*;
import ij.plugin.*;
import ij.plugin.frame.*;

public class ROI_fLoc implements PlugIn {

        public void run(java.lang.String arg) {
                ImagePlus imp = IJ.getImage();

          ImageProcessor ip = imp.getProcessor();
          Roi a = imp.getRoi();
          imp.setRoi(a);
          ImageStatistics is = imp.getAllStatistics();
                double w = ip.getWidth();
                double h = ip.getHeight();
                Rectangle r = ip.getRoi();
                double xc = is.xCentroid;
                double yc = is.yCentroid;
                double an = is.angle;//angle of the approximate ellipse
                double ma = is.major;//lenght of the long axis of the approximate ellipse
                double mi = is.minor;//lenght of the short axis of the approximate ellipse

                IJ.log("width: " + w);
                IJ.log("height: " + h);
                IJ.log("roi:" + a);
                IJ.log("angle:" + an);

                //Convert to a unit circle
                for (int y = r.y; y<= (r.y+r.height); y++){
                for (int x = r.x; x<= (r.x+r.width); x++){
```

```
                double z;
                        if ((y == yc)&&(x == xc)){
                        z = 0;
                        } else if (y == yc){
                        double sita = Math.toRadians(an);
                        z =
2*Math.sqrt((Math.cos(sita)*Math.cos(sita)/(ma*ma)+Math.sin(sita)*Math.sin(sita)/(mi*mi))*((x-
xc)*(x-xc)+(y-yc)*(y-yc)));
                        } else if (x == xc){
                        double sita = Math.toRadians(90+an);
                        z =
2*Math.sqrt((Math.cos(sita)*Math.cos(sita)/(ma*ma)+Math.sin(sita)*Math.sin(sita)/(mi*mi))*((x-
xc)*(x-xc)+(y-yc)*(y-yc)));
                        } else {
                        double ca = Math.atan((y-yc)/(x-xc));
                        double sita = ca + Math.toRadians(an);
                        z =
2*Math.sqrt((Math.cos(sita)*Math.cos(sita)/(ma*ma)+Math.sin(sita)*Math.sin(sita)/(mi*mi))*((x-
xc)*(x-xc)+(y-yc)*(y-yc)));
                        }
            int i = ip.get(x,y);//intensity on the each pixel
                    if (i > 1){
                    IJ.log("(x,y)=" + "¥t" + x +    "¥t " + y + "¥t " + "intensity=" + "¥t "+ i + "¥t " +
"localization:" + "¥t " + z );
                    }
                    }
                }
        }
}
```